

**Cell Reports, Volume 21**

## **Supplemental Information**

### **Clonal Heterogeneity Influences**

#### **the Fate of New Adaptive Mutations**

**Ignacio Vázquez-García, Francisco Salinas, Jing Li, Andrej Fischer, Benjamin Barré, Johan Hallin, Anders Bergström, Elisa Alonso-Perez, Jonas Warringer, Ville Mustonen, and Gianni Liti**

# Supplemental Information

## Supplemental Experimental Procedures

1	Experimental methods . . . . .
1.1	Random and targeted clone isolation . . . . .
1.2	Engineered genetic constructs . . . . .
1.3	Genetic cross . . . . .
1.4	Luria-Delbrück fluctuation assay . . . . .
1.5	Growth phenotyping . . . . .
1.6	Media composition . . . . .
2	Theory and data analysis . . . . .
2.1	Sequence analysis . . . . .
2.2	Genome-wide scan of pre-existing variants under selection . . . . .
2.3	Reconstruction of subclonal composition . . . . .
2.4	Subclonal dynamics resolved by whole-population genome sequencing . . . . .
2.5	Adaptive <i>de novo</i> mutations and genomic instability in clonal isolates . . . . .
2.6	Validation of putative driver genes . . . . .
2.7	Fitness distribution and population averaging . . . . .
2.8	Decomposition of background-averaged fitness effects of mutations . . . . .

## Supplemental Figures

## Supplemental Tables

## Supplemental References

# Supplemental Experimental Procedures

## 1 Experimental methods

### 1.1 Random and targeted clone isolation

We isolated ancestral and evolved individuals from representative selection experiments to characterize their individual genome sequences and their fitness. Each sample underwent serial dilution to attain a single-cell bottleneck. We isolated individuals from both ancestral populations (WAXNA F12 1 YPD, WAXNA F12 2 YPD) and 6 evolved populations (WAXNA F12 1 HU 2, WAXNA F12 1 HU 3, WAXNA F12 2 HU 3, WAXNA F12 1 RM 3, WAXNA F12 1 RM 4, WAXNA F12 2 RM 2) to measure the initial and final fitness distribution. 96 colonies were randomly picked from each population to span a range of fitness. We measured their growth rate using the high-resolution scanning platform described in ‘Growth phenotyping’.

Furthermore, we isolated individuals at the fitter end of the fitness distribution, possibly harboring driver mutations. Since adaptation to one environment typically results in fitness gains or losses in other environments, we profiled 96 individuals from each selection experiment with an array of 6 different environments (YPD, HU at  $10 \text{ mg mL}^{-1}$ , RM at  $0.025 \text{ g mL}^{-1}$ , galactose at 2%, heat at  $40^\circ\text{C}$  and sodium arsenite at  $1.5 \text{ mM}$ ) to discriminate cells based on their phenotypic response. After visual inspection of shared effects across environments, we tested genetic markers by PCR, digestion and targeted resequencing of *de novo* mutations identified from the genome analysis of whole populations. In the hydroxyurea experiment, a heterozygous mutation in *RNR4* was genotyped by PCR followed by *BanI* digestion. In the rapamycin experiment, heterozygous *DEP1* and *INP54 de novo* mutations were genotyped using PCR, followed by *AluI* digestion and confirmed by Sanger sequencing in a subset of samples. We chose a total of 44 clones (22 per environment) for whole-genome sequencing (Table S1).

### 1.2 Engineered genetic constructs

We selected two genes in which we found putative driver mutations in hydroxyurea (*RNR2*, *RNR4*) and five genes in rapamycin (*CTF8*, *DEP1*, *FPRI*, *TORI*, *YNR066C*), and engineered gene deletions to investigate their phenotypic effect. We also built hemizygous strains to determine the adaptive value of background variation in putative driver genes, by engineering in or out ancestral or evolved alleles in opposite backgrounds. For pre-existing variants, the test for reciprocal hemizygosity uses one-step PCR deletion with *URA3* as a selectable marker. Starting from haploid versions of the WA and NA strains (either *MATa*, *ho::HygMX*, *ura3::KanMX* or *MAT $\alpha$* , *ho::NatMX*, *ura3::KanMX*), we deleted the candidate genes and constructed all possible combinations of reciprocal hemizygous strains (Figure S6). The deletion in the haploid strain was confirmed by PCR

and then crossed with the opposite mating type to generate the hemizygous hybrid strains. To test driver *de novo* mutations, we engineered reciprocal hemizygous deletions for two clones carrying the same background allele with heterozygous *de novo* mutations in *RNR2* and *TOR1*. The gene deletion was performed using the dominant selectable marker *NatMX* and we used Sanger sequencing to identify the deleted allele (wild-type or mutated copy).

### 1.3 Genetic cross

We sought to measure the fitness contributions of pre-existing and *de novo* mutations using a library of recombinant genomes. To do so, we designed a genetic cross where both ancestral and evolved genetic backgrounds were re-shuffled in new combinations and tested for fitness with and without drugs. The genetic cross included the parents, ancestral and evolved isolates. The WA and NA haploid parents were used in *MATa*, *ura3* and *MAT $\alpha$* , *lys2* configurations. We derived haploid lines by sporulation on KAc medium from the ancestral and evolved clones. Only tetrads with four viable spores were chosen for continuation in the experiment. Spores were genotyped for mating type (*MATa*, *MAT $\alpha$* ) using tester strains and for auxotrophies (*ura3*, *lys2*) by plating on dropout medium. We chose spores from tetrad configurations with the mating marker co-segregating as *MATa*, *ura3* or *MAT $\alpha$* , *lys2*, allowing a systematic cross between all strains of opposite mating type. We then determined whether each spore inherited the wild-type or the mutated allele by Sanger sequencing of the candidate gene.

Eight ancestral haploid segregants (4 *MAT $\alpha$* , *lys2* and 4 *MATa*, *ura3*) were randomly isolated from the ancestral population. For the hydroxyurea environment, we probed individually beneficial *de novo* mutations in *RNR2* (Y169H) and *RNR4* (R34I), which reside on different chromosomes of the *S. cerevisiae* genome. The *RNR2* mutant was isolated from WAXNA F12 1 HU 3 (clone C3) and the *RNR4* mutant from WAXNA F12 2 HU 1 (clone C1) at  $t = 32$  days. For rapamycin, three evolved clones isolated at  $t = 32$  days were used: one clone with no identifiable driver from WAXNA F12 2 RM 2 (clone C1), a homozygous *FPRI* mutant (W66\*) from WAXNA F12 2 RM 1 (clone C3); and a heterozygous *TOR1* mutant (W2038L) from WAXNA F12 1 RM 2 (clone C3). For the hydroxyurea experiment, 21 tetrads were taken for crossing (12 for *RNR2* and 9 for *RNR4*) resulting in 84 spores. For the rapamycin environment, 25 tetrads were used (1 without driver, 4 for *FPRI*, 20 for *TOR1*), resulting in 100 spores.

A genetic cross of size  $48 \times 48$  in hydroxyurea yielded 2,304 hybrids, and  $56 \times 56$  in rapamycin, giving 3,136 hybrids. We performed the genetic cross using the Singer RoToR HDA robot on YPD plates (see ‘Media composition’). Subsequently, the hybrid populations were grown for two rounds on minimal medium to ensure colonies of solely diploid cells and avoid haploid leakage. A small number of crosses were not successful due to mating inefficiency or slow growth (56 in hydroxyurea and 654 in rapamycin), leaving a total of 2,248 and 2,482 hybrids, respectively. This

was due to mistyping of the mating locus in one *FPRI* spore and three *TORI* spores, which were excluded together with their derived hybrids. Phenotypic measurements of the crosses were carried out using the high-throughput method of yeast colony growth described in ‘Growth phenotyping’.

#### 1.4 Luria-Delbrück fluctuation assay

We performed a fluctuation test to determine the rate of loss-of-heterozygosity (LOH) in different backgrounds, by following the loss of a heterozygous *URA3* marker that results in 5-FOA resistant colonies (Lang and Murray, 2008; Luria and Delbrück, 1943). In all strains tested the *URA3* gene was deleted from its native location in chromosome V and inserted in the *lys2* locus (*lys2::URA3*) in chromosome II (~470 kb). This genotype is the same used in the crossing phase and therefore shared by all individuals in the population. Our system does not have dedicated markers to distinguish different mechanisms leading to LOH but instead gives an aggregate measurement of the total LOH rate at the *URA3* locus (Figure 5B). The strains were first patched in dropout medium minus uracil and then streaked for single colonies in plates with YPD or YPD supplemented with the drugs (HU at 10 mg mL<sup>-1</sup> or RM at 0.025 g mL<sup>-1</sup>). Colonies were grown for 3 days at 30 °C. Cells were resuspended in water and cell concentration was measured by flow cytometry to obtain a correct dilution factor in the subsequent plating. Cells from each replicate were plated in YPD to determine the total number of colony-forming units (CFUs), and in 5-FOA plates (1 g L<sup>-1</sup>) to count the number of *URA3*-defective CFUs. For each genetic background, we confirmed the loss of the *URA3* marker in 96 colonies by diagnostic PCR. Four replicates per experiment were used to determine the LOH rate.

To ensure the absence of meiotic spores we inspected ~100 cells per sample. This control was introduced for two reasons. First, the NA parent is a very fast and efficient sporulator (Gerke et al., 2006). We observed the induction of meiosis even without the specific KAc environmental signal required in the laboratory strain S288C (and its derivatives) to initiate sporulation. Second, rapamycin has been shown to promote sporulation by modulating the nutrient sensing pathway (Zheng and Schreiber, 1997). In contrast, hydroxyurea is a very potent meiotic inhibitor. We did not observe fully formed meiotic spores throughout the experiment, though we cannot exclude that meiotic events before the meiotic commitment point (e.g. double-strand breaks) may have occurred that could affect the LOH rate. Therefore, whilst meiotic sporulation can play an adaptive role to reveal recessive mutations (Figure 5), it is most likely neutral on its own in both stress environments.

#### 1.5 Growth phenotyping

To carry out phenotype measurements we used a high-resolution scanning platform, Scan-o-matic, to monitor growth in a 1,536-colony design on solid agar medium (Zackrisson et al., 2016). Solid

media plates designed for use with the Singer RoToR HDA robot (Singer Ltd) were used throughout the experiment. Casting was performed on a leveled surface, drying for  $\sim 1$  day. We designed a randomized experimental layout by distributing genotypes of interest over 1,152 positions across each plate, keeping every fourth position for 384 controls used for removal of spatial bias. Controls were interleaved in the pre-culture step using a custom-made RoToR pinning program.

We recorded phenotypic measurements using high-quality desktop scanners (Epson Perfection V700 PHOTO scanners, Epson Corporation, UK) connected via USB to a standard desktop computer. Scanner power supplies were separately controlled by power managers (GEMBIRD EnerGenie PowerManager LAN, Gembird Ltd, Netherlands) that immediately shut down the scanner lamp between scans. Images were acquired using SANE (Scanner Access Now Easy). We performed transmissive scanning at 600 dpi using 8-bit grey scale, capturing four plates per image. Plates were fixed by custom-made acrylic glass fixtures. Orientation markers ensured exact software recognition of fixture position. Each fixture was calibrated by the scanner using a calibration model that provided positions for each feature of the fixture, relative to its orientation markers. Pixel intensities were normalized and standardized across instruments using transmissive scale calibration targets (Kodak Professional Q-60 Color Input Target, Kodak Company, USA). Scanners were maintained in a high-humidity environment at 30 °C (incubation room) and kept covered in custom-made boxes during experiments to avoid light influx and minimize evaporation.

Experiments were run for 3 days and scans were continuously performed every 20 minutes. Each image stack was processed in a two-pass analysis. The first-pass was performed during image acquisition and was responsible for setting up the information needed for growth estimations. Positions in each image were matched to the fixed calibration model using the fixture orientation markers, allowing detection and annotation of plates and transmissive scale calibration strips. In the second-pass analysis, images were segmented to identify the location of the plate and the transmissive scale calibration strip. The calibration strips were trimmed and the pixel intensities compared to the manufacturer's supplied values, such that normalized pixel values remained independent of fluctuations in scanner properties over time and space. The colonies were detected using a virtual grid across each plate based on pinning format, and the grid was adjusted for the intersections to match the center of the features detected. At every intersection, each colony and the surrounding area were segmented to determine the local background and pixel intensities. Differences in pixel intensity were converted to population size estimates by calibration to independent cell number estimates (spectrometer and FACS). Based on these, we obtained growth curves in physical units.

Raw measurements of population size  $n(t)$  were smoothed in a two-step procedure. First, a median filter identified and removed local spikes in each curve. Second, a Gaussian filter reduced the influence of remaining local noise. Since we expect a population to double in size during the average time taken to progress through the cell cycle, we use an exponential growth model defined

as  $n(t) = n(0)e^{\lambda t}$ , where  $\lambda$  is the absolute growth rate. If the time that has passed is exactly the doubling time  $\tau$ , it is trivial to show that within this time span the growth rate can be rewritten as  $\lambda = \frac{\ln 2}{\tau}$ . It then follows that the absolute growth rate  $\lambda$  can be obtained from the linear fit of any two log-transformed measurements of  $n(t)$  in exponential phase, according to  $\lambda = \frac{\ln n(t_f)/\ln n(t_i)}{t_f - t_i}$ . Therefore, we define the absolute growth rate as the maximum rate during exponential phase, which we estimate by the steepest slope using local regression over five consecutive measurements of  $n(t)$ . For quality control, the residuals of the model are then used to determine goodness-of-fit and to flag growth curves suspected to be of poor quality, which are visually inspected for artefacts. Rejection rates averaged approximately 0.3% across experiments.

To account for systematic errors, we used an isogenic control at every fourth position in each plate. The fitter of the two parental strains (NA) was chosen as the isogenic control to ensure sustained and reproducible growth across the plate that would enable us to subtract systematic errors. We defined a two-dimensional reference matrix of the 384 controls (on each 1,536 plate) to correct for structured spatial bias in growth rate estimates. Controls with extreme values were removed and the remaining control positions were used to interpolate a normalization surface. This surface was first smoothed with a kernel filter to exclude any remaining noisy measurements, and then by Gaussian smoothing to soften the contours of the landscape. For a colony measured at position  $(i, j)$ , the absolute growth rate was rescaled by taking the log-transformed difference between the observed estimate and the growth of the normalization surface, i.e. the relative growth rate is then  $\lambda_{ij} \rightarrow \log_2 \frac{\lambda_{ij}}{\lambda_{ij}^{\text{norm}}}$ .

## 1.6 Media composition

During the crossing phase, the cells were expanded and maintained in YPD medium (1% yeast extract, 2% bacto peptone, 2% D-glucose and 1.7% agar). WAXNA F<sub>1</sub>/F<sub>11</sub> populations were sporulated in solid KAc medium (2% potassium acetate and 2% agar). WAXNA F<sub>2</sub>/F<sub>12</sub> populations were then selected in minimal medium lacking uracil and lysine (0.67% of yeast nitrogen base (YNB), 2% glucose and 0.2% of dropout mix minus uracil and lysine). The selection phase of the experiments was carried out in YPD medium supplemented with the drug. All selection experiments with drugs (as well as follow-ups) used media supplemented with hydroxyurea (HU) at 10 mg mL<sup>-1</sup> or rapamycin (RM) at 0.025 g mL<sup>-1</sup>, supplied by Sigma-Aldrich.

As part of the follow-up assays, we used antibiotic resistance as a selectable marker to engineer gene deletions and build hemizygous strains, plating in YPD supplemented with the corresponding antibiotic (see ‘Engineered genetic constructs’). We supplemented YPD medium with nourseothricin (Nat) at 100 g mL<sup>-1</sup>, hygromycin B (Hyg) at 200 g mL<sup>-1</sup> and G418 at 400 g mL<sup>-1</sup>. Transformations of reciprocal hemizygous strains also relied on *URA3* as a selectable marker and were plated in minimal medium lacking uracil (0.67% YNB, 2% glucose and 0.2% dropout mix mi-

nus uracil). The fluctuation assay was carried out in YPD, or YPD supplemented with the drug (see ‘Luria-Delbrück fluctuation assay’). Colonies defective in the *URA3* allele were selected in 5-FOA plates (YPD medium supplemented with 5-fluoroorotic acid at  $1 \text{ g mL}^{-1}$ ). In the genetic cross, the clones used were sporulated in solid KAc medium described above (see ‘Genetic cross’). Haploid strains were derived from dissected spores and genotyped for their mating type, *URA3/LYS2* auxotrophies and known *de novo* mutations. Strains were crossed in YPD and selected in minimal medium depleted of uracil and lysine.

Growth phenotyping was performed on solid medium using Singer PlusPlates (Singer Ltd). Each plate was cast with 50 mL of synthetic complete (SC) medium, composed of 0.14% YNB, 0.5% ammonium sulphate, 0.077% Complete Supplement Mixture (CSM, ForMedium), 2% (w/v) glucose and pH buffered to 5.8 with 1% (w/v) succinic acid. The medium was supplemented with  $20 \text{ g L}^{-1}$  of agar. Due to the need for quantitative measurements we chose SC over YPD medium for phenotyping. Measurements in SC and YPD should be comparable since both environments are nutrient rich, though we cannot exclude potential interactions of SC or YPD with the different drugs. However, we deemed the potential error associated with this difference in medium to be substantially less than the error due to systematic biases when using YPD for high-throughput phenotyping (see ‘Growth phenotyping’).

## 2 Theory and data analysis

### 2.1 Sequence analysis

Short-read sequences were aligned to the *S. cerevisiae* S288C reference genome (Release R64-1-1, downloaded from the Saccharomyces Genome Database on February 5, 2011). Sequence alignment was carried out with Stampy v1.0.23 (Lunter and Goodson, 2011) and local realignment using BWA v0.7.12 (Li and Durbin, 2009). After removing PCR duplicates, the median genome-wide DNA coverage was  $94\times$  across whole-population samples,  $23\times$  across ancestral isolates and  $30\times$  across evolved isolates (ranging from  $9\times$  to  $150\times$ ; first quartile  $24\times$  and third quartile  $91\times$ ).

We detected single-nucleotide variants where the WA and NA parents differ, which comprises the background variation segregating in the cross (52,466 sites). We obtained allele counts on these loci using GATK UnifiedGenotyper v3.5-0-g36282e4 (DePristo et al., 2011). These counts were polarized to report WA alleles at each locus, as neither of the parents is the reference genome. The allele counts for segregating variants were first processed using the filterHD algorithm, which takes into account persistence along the genome due to linkage and allows for jumps in allele frequency if there are emerging subclones in the populations.

To detect *de novo* mutations we used three different algorithms: GATK UnifiedGenotyper v3.5-0-g36282e4 (DePristo et al., 2011), Platypus v0.7.9.1 (Rimmer et al., 2014) and SAMtools v1.2-10



(Li, 2011). We focused on single-nucleotide variants (SNVs) and small insertions and deletions (indels). We first performed calling of both SNVs and indels for all ancestral isolates, evolved isolates and the parents. Using BCFtools (Li, 2011), we subtracted parental variation from all derived samples (ancestral and evolved), and excluded variation found in ancestral isolates from all evolved samples to account for segregating variation that was missed. We then required to see a given variant in more than six reads, be covered by more than ten reads and pass the default flags for the algorithms. For clonal isolate sequences, we further required that only a single alternative allele is observed. We then used GATK UnifiedGenotyper to genotype variants identified by at least two of the algorithms. For whole-population sequences, we allowed calls reporting more than one allele and we changed Platypus filtering to allow also ‘allele bias’ calls. To detect allele frequency changes over time, we only considered loci where the minimum variant allele count across time points was less than two and the maximum more than six reads. To avoid an increase of false positives in whole-population samples, we used more stringent filters on mapping and base quality biases and goodness of fit than for isolate samples. This is particularly important in complex regions where subclonal heterogeneity (e.g. due to variation in copy number) could cause difficulties in calling mutations. Finally, to increase our sensitivity of detection of putative *de novo* variants in recurrent target genes, we kept mutations in *CTF8*, *RNR2*, *RNR4*, *FPRI* or *TORI* that were only called by a single algorithm.

## 2.2 Genome-wide scan of pre-existing variants under selection

We observed patterns of selective sweeps when a driver allele with a significant fitness advantage starts to gain in frequency due to the selective pressure applied (Figures 2 and S2). This movement also causes allele frequency changes at nearby loci containing passenger alleles that are genetically linked with the driver, in a process called genetic hitchhiking.

To discern drivers and passengers, we consider a model of a population evolving in a regime of strong selection, where there is a favored allele (driver) at locus  $i$ , and a set of linked passengers. We have previously developed a computational approach to analyze selection acting on pre-existing genetic variation that results from a cross (Illingworth et al., 2012). Genetic drift plays a negligible role for allele frequency changes in the selection phase as the population size ( $\sim 10^7$  cells) is much larger than its duration ( $\sim 54$  generations). Therefore, we can assume that the allele frequencies change deterministically and the remaining noise is due to sampling caused by finite sequencing depth.

A selective sweep is then well approximated by a model of the frequency  $x_i^{\text{WA}}$  of the WA allele at locus  $i$  which satisfies the logistic equation,

$$\frac{dx_i^{\text{WA}}}{dt} = \frac{\sigma_i}{2} x_i^{\text{WA}} (1 - x_i^{\text{WA}}). \quad (\text{S1})$$

The frequency of the NA allele at locus  $i$  is  $x_i^{\text{NA}} = 1 - x_i^{\text{WA}}$ . Here, the selection coefficient  $\sigma_i$  is the fitness difference  $f_i^{\text{WA}} - f_i^{\text{NA}}$  between the alleles, and the pre-factor reflects a diploid population with additive selection. This growth model is a deterministic approximation to the stochastic evolution of  $x_i(t)$ , which is commonly described by the Wright-Fisher model with directional selection.

To account for the effects of linkage between mutations, we consider a model with two alleles possible at each locus, in which the driver mutation is at locus  $i$  and passengers at loci  $j$ . We refer to the two alleles at the  $i$  locus as  $a \in \{\text{WA}, \text{NA}\}$ , and the alleles at the  $j$  loci as  $b \in \{\text{WA}, \text{NA}\}$ .

According to our model, the dynamics of passenger alleles are fully specified by the motion of the local driver. The effect of the selected allele on existing variation at a passenger locus  $j$  is given by

$$x_j^b(t) = \sum_{a \in \{0,1\}} x_i^a(t) \frac{x_{ij}^{ab}(t_0)}{x_i^a(t_0)}, \quad \text{with } j \neq i \quad (\text{S2})$$

where the two-locus haplotype frequency is  $x_{ij}^{ab}(t_0) = x_i^a(t_0)x_j^b(t_0) + (-1)^{a+b}D_{ij}$ , and  $D_{ij}$  denotes linkage disequilibrium.

We note that due to short-read sequencing of a mixed population we cannot directly measure the two-locus haplotype frequency  $x_{ij}^{ab}$  or linkage disequilibrium  $D_{ij}$ , but we can parameterize  $D_{ij}$  in terms of the recombination which took place during the crossing phase. After  $N_c$  generations of sexual recombination, linkage disequilibrium is given by  $D_{ij}(t) = (1 - \rho_{\text{tot}})^{N_c} D_{ij}(t_0)$ , where the total recombination rate depends on the distance between the loci  $\Delta_{ij}$  in base pairs (bp) and the local recombination rate  $\rho$  in units of  $\text{bp}^{-1} \text{gen}^{-1}$ .

Therefore for a given driver locus and a set of passengers the model is fully specified by the strength of selection, the pairwise linkage structure (or recombination landscape), and allele frequencies at both driver and passenger loci at  $t=0$  days.

We learn these parameters via a maximum likelihood approach with a binomial noise model accounting for sequencing noise. We would like to carry out a systematic driver scan, rather than using a search heuristic for proposing candidate driver locations. To achieve this, we first parameterized the linkage structure with a recombination landscape inferred for this cross in a separate study (Illingworth et al., 2013), avoiding the need to estimate a local recombination rate from allele frequency changes. Secondly, we use the posterior mean of the allele frequency at  $t=0$  days, as obtained with the filterHD algorithm, to fix the initial condition. Setting the initial frequency factors out any frequency deviations of either allele that took place during the crossing phase, which are due to selection on differential mating efficiency. As a result, for each driver-passenger model we only need to learn the strength of selection and we can therefore systematically scan through each of the 52,466 segregating sites, testing the alleles at each locus to be under selection. The

resulting log-likelihood score is compared to a null model where selection on the driver locus is set to zero. This null model corresponds to no frequency changes during the experiment and does not have any parameters to be learned.

We performed a systematic driver scan including passengers within variable window sizes  $\pm 2$  kb, 5 kb, 10 kb, 30 kb, 50 kb. Emerging subclones result in global allele frequency changes that supersede the local signal, which is the hallmark of selection acting on pre-existing variation. In consequence, we only considered time points when populations had not yet become clonal, up to  $t=4$  days. For each scan we selected the top 200 loci (out of 52,466) and then required that a given window was identified to be among the top scoring ones in at least two populations. The remaining windows were merged if their passenger loci overlapped. Finally, we required that the region was not identified among those scoring highly in the control environment.

The scan identified a region of interest for rapamycin resistance, found in chromosome VIII (460–490 kb) as discussed in the main text. The signal is visible in all rapamycin populations but not in the control. However, we were not able to localize it fully due to a low recombination rate in this region and possibly also caused by the presence of multiple drivers. The top hits with different passenger window sizes show substructure in terms of peak location. Smaller windows contain multiple peaks, which then get merged to single peaks in larger windows. We note that theoretically the passenger window size should not matter provided the linkage model is adequate and there are no multiple drivers affecting the passenger dynamics. In summary, the region as a whole has strong support across populations to contain pre-existing variation where NA allele(s) are beneficial in rapamycin, albeit we cannot statistically map the signal more finely. We followed up two candidate genes in the region (*CTF8* and *KOG1*), and we validated *CTF8* to have a resistance phenotype (see ‘Validation of putative driver genes’). *KOG1*, which is part of the target-of-rapamycin (TOR) pathway, harbors pre-existing missense variants in the population and is thus a plausible target of selection. We did not find regions that replicated across all populations in hydroxyurea.

### **2.3 Reconstruction of subclonal composition**

In the late stages of the selection experiment we identified global allele frequencies changes of pre-existing, segregating variants caused by one or multiple *de novo* mutations (or a particularly favorable combination of the background variation itself) in subclones that are under positive selection. During the selection phase, which is asexual, mutations in the genome of a cell are physically linked. Thus after a cell acquires a beneficial *de novo* mutation this can outweigh all its background variants, which become passengers (they may of course contribute to the fitness of that cell as well). At the genomic level, such an expanding subclone leaves a large imprint on the data at polymorphic sites, with long-range correlations reflecting the genotype of the cell hit by the beneficial *de novo* mutation. This signal with global, long-range correlations and sudden jumps

corresponding to the expanding genotype is qualitatively different from the signal resulting from the localized sweep picture discussed in the previous section.

In this section, we describe how we extend and use the cloneHD algorithm (Fischer et al., 2014) to reconstruct the emerging subclone dynamics in a cell population. The cloneHD algorithm was developed to explain data from short-read DNA sequencing experiments of mixed cell populations (read depth and variant counts) under the following assumptions: (i) The cells evolve asexually (without recombination). This ensures that there are long-range correlations along the genome, which can, in principle, be reconstructed from short-read data. (ii) The population consists of a mixture of subclones, i.e. groups of genetically identical cells. The total number of subclones and their relative fractions in the population are unknown. The number of subclones, which can be reconstructed from real data, is small and depends on how different they are and what their population fractions are. (iii) Each subclone carries a unique copy number profile and genotype. Both of which are unknown. (iv) There is a distinct bulk component of the population which differs from the subclones, e.g. by having a different set of genotypes. Its fraction is also unknown. (v) When several samples are jointly analyzed, the same subclonal populations are assumed to be present in all samples. However, their frequencies in some of the samples can be zero.

Previously, cloneHD was used to explain subclonal heterogeneity found in human cancers. With a few extensions, this methodology can also be used for the yeast evolution experiment studied here. After the crossing phase, the populations evolve asexually under selective pressure. The rounds of crossing of the two original strains have produced a diverse pool of recombinants, where the genotype of each cell is – for all practical purposes – unique. This ancestral population of diploid cells is modeled here as the bulk component. Its allele frequency profile can be seen in Figures 2 and S2.

At the later stages of the evolution, a small number of individual yeast cells start to outgrow the rest of the population, maybe due to a beneficial combination of pre-existing variation or due to *de novo* mutations. These cells grow clonally to measurable fractions of the population and leave their fingerprint in the allele frequency profile genome wide. In the extreme case, a single cell grows clonally to take over the entire population and its individual genotype that can be directly observed in the sequencing data. In the general case, there will be a mixture of subclones and bulk population as described above. As an added complication, subclone copy number profiles need not be pure diploid.

This scenario is already covered in principle in the model underlying cloneHD (see Section 4 in the Supplemental Information of Fischer et al. (2014)). In the current study, the population is sequenced at several time points such that there are multiple related samples available for inference

with cloneHD. For the read depth  $N_i^t$  at locus  $i$  and time point  $t$ , the emission probability is

$$N_i^t \sim \text{Pois}(N_i^t | M^t \langle c \rangle_i^t), \quad (\text{S3})$$

$$\text{with } \langle c \rangle_i^t \equiv c_0 (1 - F^t) + \sum_{j=1}^n c_{ij} f_j^t \quad (\text{S4})$$

where  $M^t$  is the mean sequencing depth per haploid DNA,  $c_{ij}^t$  is the total copy number of subclone  $j$  at locus  $i$ ,  $c_0$  is the total copy number of the reference compartment (2 for diploid) and  $f_j^t$  is the frequency of subclone  $j$  (with  $F^t \equiv \sum_{j=1}^n f_j^t$ ).

The number of WA reads  $n_i^t$  determines the observed allele frequency  $x_i^t$  and is assumed to be binomially distributed

$$x_i^t \approx \frac{n_i^t}{N_i^t}, \quad \text{with } n_i^t \sim \text{Bin}(n_i^t | N_i^t, x_i^t) \quad (\text{S5})$$

$$\text{where } x_i^t \equiv \frac{\langle g \rangle_i^t}{\langle c \rangle_i^t}, \quad \text{with } \langle g \rangle_i^s \equiv x_i^{t_0} (1 - F^t) + \sum_{j=1}^n g_{ij} f_j^s \quad (\text{S6})$$

where  $g_{ij}$  is the genotype of subclone  $j$  at locus  $i$  and  $x_i^{t_0}$  is the initial allele frequency spectrum. The only substantial difference to the situation in the cancer setup is that here the genotype of a particular subclone  $j$  is persistent across large regions of the yeast genome, reflecting the haplotype structure resulting from the cross. In cancer, these correlations along the genome are missing since the aforementioned model is only applied to somatic point mutations which occur randomly along the genome. Altogether, the subclonal structure of the yeast cell populations can be reconstructed with cloneHD in cna+snv mode, where both the CNA and SNV data are modeled with persistence along the genome. The rest of the cloneHD workflow fully applies. First, the read depth and the allele frequency data are analyzed with filterHD, thus finding a segmentation of both data tracks for all samples jointly (in later stages subclones are larger and the transition points become more prominent). This information and the initial allele frequency profile  $x_i^{t_0}$  are provided to cloneHD together with the read depth and pre-existing variant allele data in cna+snv mode. The maximum likelihood set of subclonal genomes (including their copy number profiles and genotypes) and their cell fractions is then found by cloneHD at each time point. Figure S1 shows the general setup and the cloneHD reconstruction for simulated data in one population.

We assessed the ability of our algorithm to recover several features of interest from simulated jump-diffusion processes over a range of plausible parameters. For each parameter set, we simulate a 1 Mb region with  $L = 10,000$  observations and 60 reads per locus on average, then compute maximum likelihood estimates using different numbers of subclones. Our choice of jump probability for simulated data is set to  $4 \times 10^{-5}$  per base. This reflects the size of linkage blocks with plausible recombination scenarios during crossing. The clones are added in a chosen background

assuming the bulk has reached a steady profile. We would like to reconstruct three features: (i) the total number of subclones, (ii) their subclonal frequency, and (iii) obtain posterior estimates of subclonal genotypes.

The maximum-likelihood estimates of the subclonal fractions are approximately equal to the true values. The reconstruction is shown in Figure S1B as a black solid line, which is the cloneHD solution for the mean posterior SNV emission rate. We can recapitulate the correct number of breakpoints and their location. The fidelity of our reconstruction to the true subclonal genotype is corroborated by the close correlation between our estimates from whole-population sequencing and the true genotypes derived from clonal isolates.

## 2.4 Subclonal dynamics resolved by whole-population genome sequencing

To reconstruct the subclonal composition of each WAxNA replicate from whole-population sequencing, we used cloneHD providing the jumps found by filterHD and the posterior mean allele frequencies of the ancestral population to act as a bulk component for the inference (see ‘Reconstruction of subclonal composition’). We used cloneHD in snv mode, as visual inspection did not reveal copy-number aberrations from whole-population sequencing. For each population, we systematically tested 0–4 subclones and determined the total data likelihoods under each model. The number of subclones per population are summarized in Table S1, together with the time evolution of subclone frequencies in Figure S3. We required a log-likelihood gain greater than 20,000 units for the inclusion of an additional subclone. This conservative cut-off only allows genome-wide signals to be associated with a subclone. This is necessary as the bulk component of the population can also change throughout the experiment. This prevents that, with a less conservative cut-off, other solutions would be favored that would introduce artifactual subclones with suitable genotypes to improve fits in regions where selection acts on the bulk (see ‘Genome-wide scan of pre-existing variants under selection’).

To ascertain the expansion of subclones throughout the experiment, we determined the allele frequency of *de novo* mutations in WA, NA and WAxNA populations during the selection phase from whole-population sequencing. We found that these mutations typically did not reach detectable frequency (i.e. between 1–5%) until more than 8 days had passed, with steady increases thereafter (Figures S3 and S4). Across populations, we found 66 point mutations by whole-population sequencing spanning 41 unique loci, out of which 50 fall onto coding sequence. These loci contain 32 functional driver mutations: 4 in *RNR2*, 10 in *RNR4*, 11 in *FPRI*, and 7 in *TORI*. This includes two tri-allelic loci: one corresponding to *FPRI* driver mutations W66\* and W66S, and another to a SNV and an insertion in *FPRI*.

## 2.5 Adaptive *de novo* mutations and genomic instability in clonal isolates

Overall, we identified 91 SNVs and indels in 173 ancestral haploid isolates, and 140 SNVs and indels in 44 evolved diploid isolates. We detected 82 SNVs and 1 insertion across 22 evolved isolates in hydroxyurea (range 1–8 per isolate), containing 10 adaptive mutations in *RNR2* and 12 in *RNR4* (Figure 4A). There were 56 SNVs and 1 deletion across 22 evolved isolates in rapamycin (range 0–6 per isolate), which contained 8 adaptive mutations in *FPR1* and 5 in *TOR1* (Figure 4B). 33 out of 36 mutations detected by whole-population sequencing across WAXNA populations could be found in clonal isolates. All *de novo* driver mutations found by clone sequencing were confirmed by targeted Sanger sequencing. Assuming the ancestral genomes to have passed through  $\sim 150$  generations during the crossing phase, we estimated a point mutation rate  $\mu = 2.89 \times 10^{-10}$  per base per generation; and similarly for evolved genomes going through  $\sim 54$  generations in the selection phase ( $\mu = 5.32 \times 10^{-9} \text{ bp}^{-1} \text{ gen}^{-1}$ ). We detected two instances of cross-contamination between populations, so the derived events in clones isolated from these populations are valid to estimate the mutation rate but should not be counted to have arisen independently.

Sequence analysis revealed that 3 out of 4 unique variants in *RNR2* (N151H, E154G and Y169H) and 2 out of 3 unique variants in *RNR4* (R34G/I) mapped to a conserved domain of the ribonucleotide-diphosphate reductase small chain. *FPR1* mutations occurred at W66, either introducing a premature stop codon or changing to serine. Previous studies indicate that the majority of non-synonymous changes in *FPR1* affect protein stability (Koser et al., 1993). Furthermore, the premature stop at W66 truncated the residue required for rapamycin binding (Y89). We observed clones carrying the W66\* mutation selected multiple times from the same founder population indicating a pre-existent individual carrying a heterozygous mutation and independent LOH events that render the loss-of-function mutation homozygous (Figure 4B). All five driver SNVs in *TOR1* (S1972I/R, W2038L/C and F2045L) mapped to the FKBP12-rapamycin-binding (FRB) domain, which is  $\sim 100$  aa long, providing a mechanistic explanation of the drug resistance (Figure 4B). Previous studies have found dominant mutations in S1972 and equivalent mutations in the mammalian TOR (mTOR) have a similar effect on drug binding. Substitutions at W2038 with a similar dominant effect are equivalent by homology to those previously described in *TOR2* (W2042) (Lorenz and Heitman, 1995).

To identify copy-number aberrations from clone sequencing, we segmented the coverage depth as a function of genomic position with cloneHD. We found one copy number gain ( $n > 2n$ ) of chromosome IX in ancestral haploid isolates. Evolved diploid isolates accrued copy number gains ( $2n > 3n$ ) in chromosomes VIII, IX and X in hydroxyurea and chromosome IX in rapamycin, as well as whole-genome copy loss ( $2n > n$ ) in rapamycin.

Using background variants as markers, we could detect mis-segregation of chromosomes leading to loss-of-heterozygosity. The presence or absence of the WA or the NA allele provides a

robust signal of heterozygosity or LOH that is not affected by sampling noise in coverage. We used cloneHD to genotype the sequenced isolate samples at segregating sites. We then grouped isolate sequences by subclone lineage, requiring at least 80% genotype similarity to belong to the same lineage. In hydroxyurea, this resulted in 22 isolates stemming from 8 subclone lineages, with more than a single isolate each. In rapamycin, 22 isolates were assigned to 4 subclone lineages, with more than a single isolate each. For each subclone lineage, we inferred its ancestral genotype. In case of a locus with a unique genotype across all isolates we assigned this to be the ancestral state. In all other cases we inferred the ancestral state to be heterozygous, as lost alleles cannot be regained. We then annotated all the isolates from each clone for LOH events. Figure 4 shows the inferred ancestral genotypes and the derived SNVs, indels, LOH events and copy number variants, grouped by population and subclone lineage. Whilst we did not find evidence of copy-number aberrations to be adaptive, we characterized fitness increases associated with LOH caused by changes in the allelic state of pre-existing and *de novo* variants (Figure 3B). To determine the rate of LOH events, we counted the number of independent events within a chromosome that have led to the gain or loss of the ancestral allele in the evolved isolate sequences. This estimate is challenging given that the ancestral states contain both homozygous and heterozygous loci, so that the precise end points of individual LOH events are uncertain. To obtain a lower bound, we counted whether any isolate had undergone LOH affecting  $\geq 10$  consecutive background variants, for each chromosome in each clone. We found 48 events in hydroxyurea and 24 events in rapamycin (6 per genome per clone). We excluded two haploid individuals from this counting as well as from the length distribution of homozygosity tracts in Figure 5A.

We compared our genome-wide estimates of the point mutation and LOH rates based on the mutation counts in clone genome sequences with locus-specific measurements of the LOH rate using a fluctuation test (see ‘Luria-Delbrück fluctuation assay’). We fitted the fluctuation data to a model of the Luria-Delbrück distribution. We determined the average number of LOH events per culture  $m$ , such that LOH rate can be estimated by  $\mu = \frac{m}{N}$ , where  $N$  is the average number of cells per culture. To determine the mean number of LOH events  $m$ , we used the probability generating function of the Luria-Delbrück distribution defined by Hamon and Ycart (2012). In the control environment, we observed a rate of  $\mu = 2.59 \times 10^{-5}$  per generation in the NA background, consistent with previous reports (Barbera and Petes, 2006). We observed an intermediate rate in the WA background ( $\mu = 8.01 \times 10^{-6} \text{ gen}^{-1}$ ) and the WAXNA F<sub>1</sub> hybrid had an approximately ten-fold lower rate ( $\mu = 4.01 \times 10^{-6} \text{ gen}^{-1}$ ). These data indicate that LOH rates can vary between genetic backgrounds. There was a sharp increase of LOH rates when colonies were grown in hydroxyurea, irrespective of the background tested. This finding is consistent with previous studies in the laboratory strain S288C reporting that replication stress promotes recombinogenic DNA lesions (Barbera and Petes, 2006). We also observed a background-dependent increase in LOH rate



in the presence of rapamycin, especially in the NA founder. Our estimates of the point mutation rate based on the mutation counts in ancestral and evolved clones ( $\sim 10^{-10} \text{ bp}^{-1} \text{ gen}^{-1}$ ) and of the LOH rate based on the fluctuation assay ( $\sim 10^{-5} \text{ gen}^{-1}$ ), suggest that any recessive genes will be likely to lose the wild-type allele by LOH. Given that the LOH rate is much higher than the point mutation rate and it typically affects large regions (100-1,000 kb, see Figure 5A), recessive mutations can feasibly be ‘rescued’ by LOH.

## 2.6 Validation of putative driver genes

To test candidate driver mutations, we measured the growth rate of engineered gene deletions to confirm whether their knockouts are beneficial. We also measured the growth of hemizygous strains to test allelic differences in driver genes with pre-existing and newly acquired mutations. The engineered genetic constructs are listed in Supplemental Tables. We performed  $n_r = 64$  replicate measurements of each construct in two independent runs, which were initiated from a single pre-culture plate, evenly distributed over 16 experimental plates and simultaneously run in 4 scanners. The growth rate of each of these strains is shown in Figures S7 and S8, labeled by genetic background  $b$  and genotype  $g$ .

We deleted one copy of *RNR2* in WA and NA diploids and sporulation of these strains resulted in tetrads with two viable spores and two unviable *rnr2Δ* mutants, indicating that this gene is essential in both backgrounds. *RNR2* is also essential in the laboratory S288C background. Furthermore, the heterozygous deletions of *RNR2* diploids show strong haploinsufficiency for hydroxyurea resistance (Figure S7). In contrast to its interaction partner, *RNR4* is not essential in the laboratory background. However, deletion of this gene in diploid WA and NA backgrounds proved it to be essential in the WA background. The NA strain is viable after deletion, though with severe growth defects. Diploid hemizygous strains for *RNR4* deletions in both backgrounds show increased sensitivity due to dosage effects (Figure S7).

*FPR1* and *TOR1* are not essential genes and we performed deletions in both haploids and diploids. *FPR1* directly binds rapamycin inhibiting the TOR pathway and its deletion is highly resistant (Figure S8). Deletion of one copy of *FPR1* does not increase the growth rate in rapamycin, indicating that both copies of the gene need to be inactivated to drive resistance. Consistently with this observation, all mutations observed in *FPR1* are homozygous. Large colonies in the *FPR1* plating assay all acquired double-hit events (*de novo* SNV or indel plus LOH) that inactivated both functional copies of the gene (inset in Figure S8). Estimates of the number of colonies for parent and hybrid backgrounds follow a similar trend to the estimates obtained with the fluctuation test. In contrast, *TOR1* deletion results in high sensitivity to rapamycin and a single deleted copy does not alter the drug response (Figure S8).

Reciprocal hemizygosity tests in ancestral hybrids confirmed background-dependent effects in

*CTF8*, with strong positive selection acting on the NA allele as predicted by our model of driver-passenger dynamics (Figure S8). *KOG1*, which is a component of the TOR signaling pathway, did not show any allelic differences but deleting either copy caused haploinsufficiency in rapamycin. We also deleted either the wild-type or the mutated allele of evolved mutant clones, generating pairs of clones identical throughout the genome except for the candidate driver mutation. The four genes harboring *de novo* driver mutations do not appear to show allelic differences between the two parental backgrounds as shown by the reciprocal hemizyosity test (Figure S8). No allelic differences were observed for *DEP1*, *INP54* and *YNR066C*, which are confirmed as passengers.

## 2.7 Fitness distribution and population averaging

To characterize the fitness of cells in a heterogeneous population with multiple subclones, i.e. where several haplotypes may be present, we measured the growth properties of an ensemble of cells. With an ensemble method, we will typically measure the population average. However, since we found subclones co-existing, these may be found in states that are far from the population mean. Hence, we determined the intra-population growth rate of the populations at the start and the end of the selection phase (Figures 3 and S9). For each population, we estimated the probability distribution  $P(\lambda^t)$  of the growth rate  $\lambda$  at time  $t$  by sampling  $n_k$  isogenic individuals. With an ensemble of  $n_k=96$  individuals per time point we took  $n_r=32$  replicate measurements per individual. The replicates were measured in two independent runs, evenly distributed over 16 experimental plates which were initiated from a single pre-culture plate and run in 4 scanners, all in parallel.

We modeled the probability distribution of the data,  $\{\lambda_n^t\}_{n=1}^{n_k}$ , as a mixture model of normal distributions,

$$P(\lambda^t) = \sum_{k=1}^K \pi_k \mathcal{N}(\lambda^t | \mu_k, \sigma_k^2), \quad (\text{S7})$$

where  $K$  is the number of components. We can interpret the mixing coefficients,  $\pi$ , as the bulk and multiple clonal components. We determined the fraction of cells in the fitter, faster clonal state(s) and the slower, bulk component by fitting  $p(\lambda)$  to a mixture of normal distributions with  $K \in \{1, 2, 3\}$  components. There are  $2K + 1$  fitting parameters, which are learned by maximizing the likelihood function  $P(\lambda^t)$ : the component means  $\{\mu_k\}$  and variances  $\{\sigma_k^2\}$ , and the relative weights between them. In multimodal populations, the weights are in good agreement with the average of two consecutive inflection points surrounding the trough between the bulk and the clonal subpopulations (Figure S9).

## 2.8 Decomposition of background-averaged fitness effects of mutations

We carried out a genetic cross to reconstruct a fraction of the genotypes that a population can explore and examined the average mutational effect of beneficial variants in multiple genetic back-

grounds. We isolated isogenic individuals from parents, ancestral and evolved populations. As described in the ‘Genetic cross’ section, we sporulated these diploid cells and selected haploid segregants of each mating type (48 in hydroxyurea and 56 in rapamycin), parameterized by an index  $a$  or  $\alpha$ . We crossed the  $MATa$  and  $MAT\alpha$  versions to create hybrids. The cross forms a two-dimensional lattice that is conveniently parameterized by the set of lattice positions  $(a, \alpha)$ .

We obtained a set of measurements for the growth rate  $\lambda$  of individuals, each of which has a unique combination of background genotype  $b$ , *de novo* genotype  $d$ , sampling time  $t$  and auxotrophy  $x$ . Every haploid genome being crossed is an independent background indexed by  $b_{\{a,\alpha\}} = 1, 2, \dots, n_b$  ( $n_b = 48$  in HU and  $n_b = 56$  in RM, either  $a$  or  $\alpha$ ), such that reshuffled diploid hybrids are parameterized by  $b_{a\alpha}$ . Genetic backgrounds are sampled before the cross (parents), before selection starts at  $t = 0$  (ancestral) or after  $t = 32$  days (evolved), such that  $t_{\{a,\alpha\}} = 1, 2, \dots, n_t$  ( $n_t = 2$  for the parents;  $n_t = 4$  at  $t = 0$ ;  $n_t = 42$  in HU and  $n_t = 46$  in RM at  $t = 32$ ). We denote *de novo* genotypes by  $d_{\{a,\alpha\}} = 1, 2, \dots, n_d$  ( $n_d = 12$  for *RNR2*;  $n_d = 9$  for *RNR4*;  $n_d = 1$  without driver;  $n_d = 4$  for *FPR1*,  $n_d = 20$  for *TOR1*). Haploid spores are auxotroph and segregate with the mating locus, such that  $x_{\{a,\alpha\}} \in \{ura3^-, lys2^-\}$ , whereas diploid hybrids do not have amino acid deficiencies. To estimate the measurement error, we carried out replicate measurements of each unique spore ( $n_r = 12$  in HU and  $n_r = 6$  in RM) and of each hybrid genotype combination ( $n_r = 3$ ). Replicates were initiated from the same pre-culture plate, evenly distributed over 32 plates that and run in 4 scanners, all in parallel.

The data matrix shows the fitness effect of every *de novo* genotype  $d$  at each background  $b$  sampled at time  $t$ , averaged over measurement replicates and measured relative to the ancestral population (Figure S10). Based on these measurements, we observed that *de novo* mutations are beneficial, yet their associations to genetic backgrounds have idiosyncratic effects. The effects of *de novo* mutations are mediated by background fitness as evidenced by the large phenotypic variance. We note that genetic crosses between different backgrounds need not give rise to a ‘symmetric’ phenotype data matrix, as we only enforce 2:2 segregation for the mating locus  $MATa/\alpha$ . Whilst background variants will co-segregate with the mating locus, *de novo* mutations need not.

To examine the average fitness effects of functional genotypes in hydroxyurea (*RNR2*, *RNR4*) or rapamycin (*FPR1*, *TOR1*), we calculated an ensemble average of the growth rate  $\lambda$ . The ensemble average  $\langle \lambda \rangle$  is either taken over single spore backgrounds  $b_{\{a,\alpha\}}$  or pairs of hybrid backgrounds  $b_{a\alpha}$  with different degrees of relatedness,

$$\langle \lambda \rangle_{\{a,\alpha\}}^{td} = \frac{1}{n_b} \sum_{b=1}^{n_b} \lambda_{\{a,\alpha\}}^{btd} \quad \text{and} \quad \langle \lambda \rangle_{a\alpha}^{td} = \frac{1}{n_b} \sum_{b=1}^{n_b} \lambda_{a\alpha}^{btd}, \quad (\text{S8})$$

where  $\langle \dots \rangle$  denotes the mean over genetic backgrounds. We found that, on average, *RNR2*, *RNR4* and *TOR1* mutations are dominant and highly penetrant (Figures 6D and 6F). In contrast, *FPR1* is recessive, only increases fitness when the mutation is homozygous and carries a fitness cost in the

absence of rapamycin (Figures 6F and S11D, respectively).

We partitioned the variation in fitness contributed by background and *de novo* driver mutations using linear mixed models. To model genetic backgrounds containing beneficial mutations we need to describe how likely a phenotype is in the presence or absence of any mutation. We restricted our model to pairs of individuals that are not closely related to avoid spurious correlations by population structure, so we retained ancestral and evolved individuals and excluded the parents. We are interested in the aggregate effect across all mutations within a spore or hybrid rather than the effects of individual variants. As the data represents a finite sample from the distribution of all possible genetic backgrounds, the background contribution to the phenotype is naturally modeled as a random-effect term (i.e. individual genetic backgrounds are drawn at random from a population, and the variance of the underlying distribution is to be inferred). In addition, other systematic effects that potentially contribute to fitness are modeled as fixed-effect terms: (i) time  $t$  when the individual was sampled, i.e. at  $t=0$  (ancestral) or  $t=32$  (evolved); (ii) *de novo* driver mutation status  $d$  of the individual, e.g. *FPR1* driver mutation in homozygous state; and (iii) auxotrophy, denoted by  $x$ , e.g. *ura3-* or *lys2-*. We implemented four nested linear mixed models outlined below.

**Model 1** We first considered a model where we only included the background without other effects. This means that the observed growth rate  $\lambda_b$  for a background  $b$  conditioned on the random effect taking a value  $\beta_b$  is distributed as

$$\lambda_b|_{\mathcal{B}=\beta_b} \sim \mathcal{N}(\beta_0 + \beta_b x_b, \sigma_\varepsilon^2), \quad (\text{S9})$$

where  $\beta_0$  is a shared constant baseline per background that must be inferred,  $\sigma_\varepsilon^2$  represents measurement noise,  $x_b$  is an element from the model design matrix (here 1 for each  $b$  as they all are assigned a value). Finally, the background growth rate is distributed as  $\mathcal{B} \sim \mathcal{N}(0, \Sigma^2)$  and its variance  $\Sigma^2$  is a model parameter to be inferred. We note that for each background  $b$  we have multiple measurement replicates of  $\lambda_b$ . Altogether, Model 1 has three modeling parameters,  $\beta_0$ ,  $\Sigma^2$  and  $\sigma_\varepsilon^2$ .

**Models 2, 3 and 4** Model 2 includes the same factors as Model 1, but the time of sampling  $t$  is nested as a fixed effect. Model 3 also accounts for *de novo* driver mutation status denoted by  $d$ . In addition, Model 4 includes a fixed effect accounting for amino acid deficiencies (or auxotrophy), denoted by  $x$ . Altogether the growth rate  $\lambda_{btdx}$ , conditioned on the random effect taking a value  $\beta_b$ , is distributed as:

$$\lambda_{btdx}|_{\mathcal{B}=\beta_b} \sim \mathcal{N}\left(\beta_0 + \underbrace{\beta_b x_b}_{\text{random}} + \underbrace{\beta_t x_t + \beta_d x_d + \beta_x x_x}_{\text{fixed}}, \sigma_\varepsilon^2\right), \quad (\text{S10})$$

where  $\beta_t, \beta_d, \beta_x$  are fixed-effect terms to be inferred and  $x_t, x_d, x_x$  are elements of the model design matrix. Compared to Model 1, Models 2, 3 and 4 have extra parameters  $\beta_t, \beta_d$ , and  $\beta_x$ . The number

of free parameters depends on how many unique levels each factor contains, e.g. how many driver mutations are sampled in the experiment.

The likelihood for a data vector  $\lambda$  given the full model (Model 4) can then be written as

$$\begin{aligned} P(\lambda \mid \text{model}) &= P(\lambda \mid \beta_0, \beta_t, \beta_d, \beta_x, \Sigma^2, \sigma_\varepsilon^2) \\ &= \prod_{(a, \alpha)} \prod_{r=1}^{n_r} \int P(\lambda_{btdx} \mid \beta_b, \beta_0, \beta_t, \beta_d, \beta_x, \Sigma^2, \sigma_\varepsilon^2) \\ &\quad \times P(\beta_b \mid \Sigma^2) d\beta_b \end{aligned}$$

where the integrand is the product of the probability density given by Equation S10 and the posterior distribution over the random effects.

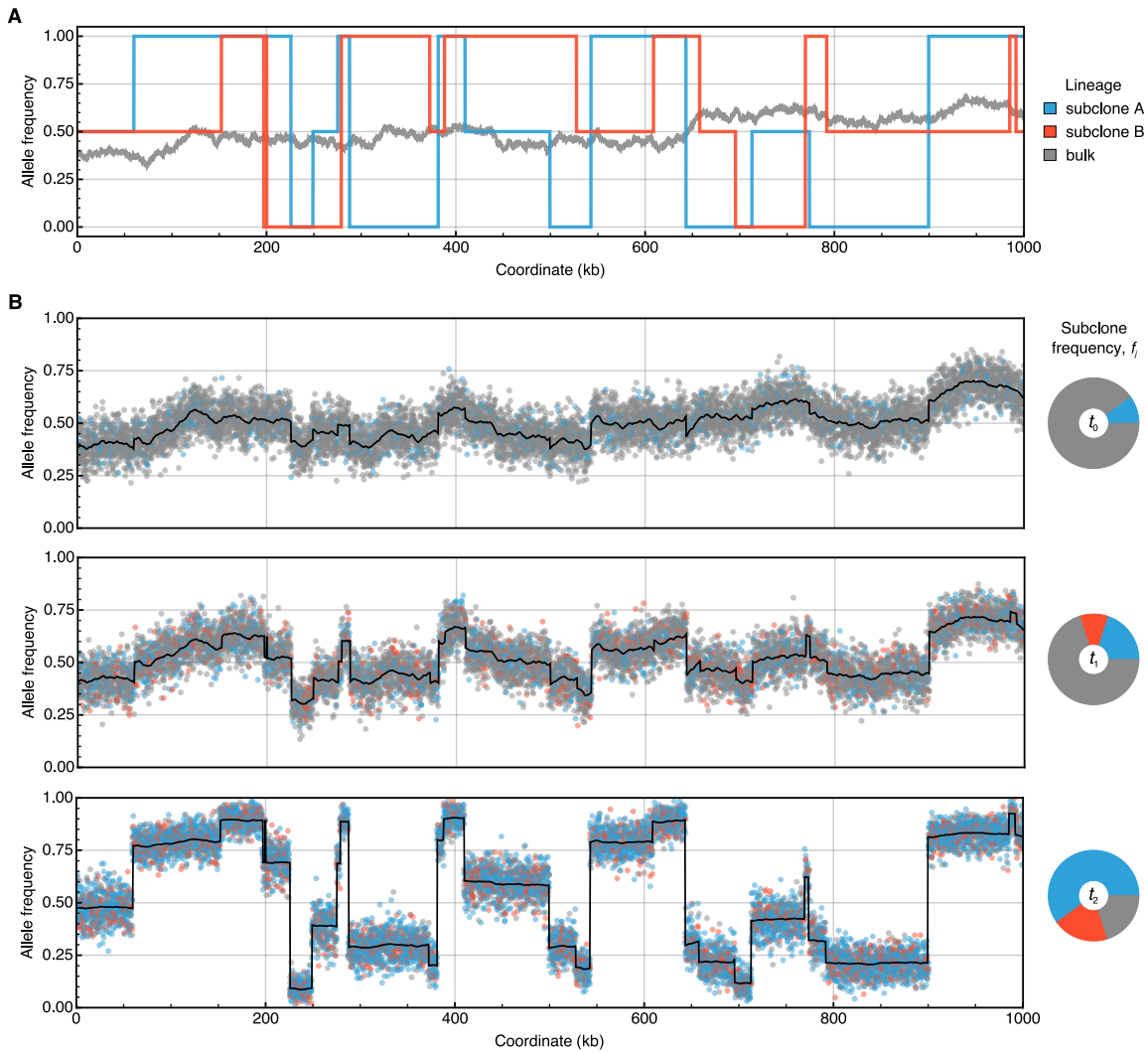
Next, we applied all four models to the phenotypes of the genetic cross: a genetic cross based on hydroxyurea selection, measured in hydroxyurea and a control environment; and a genetic cross based on rapamycin selection, measured in rapamycin and a control environment, both for spores and hybrids. We fitted each model using restricted maximum likelihood with the R-package lme4 (Bates et al., 2015), summarized in Table S2. Using Akaike's Information Criterion (AIC) for model selection all conditions had a score supporting Model 4 apart for those selected and measured in hydroxyurea, where both spores and hybrids supported Model 3. We compared the fitted and observed values and in all cases the fits were good, as shown in Figure S12 for Model 4.

We can assess the overall goodness-of-fit of the models by the proportion of variance explained. In particular, we would like to know the contribution of various model components to the overall fit, and to do so we obtain separate measures for the partial contributions of fixed and random effects (Gelman and Hill, 2006)

$$r^2 = \frac{\sigma_F^2 + \sigma_R^2}{\sigma_F^2 + \sigma_R^2 + \sigma_\varepsilon^2}, \quad (\text{S11})$$

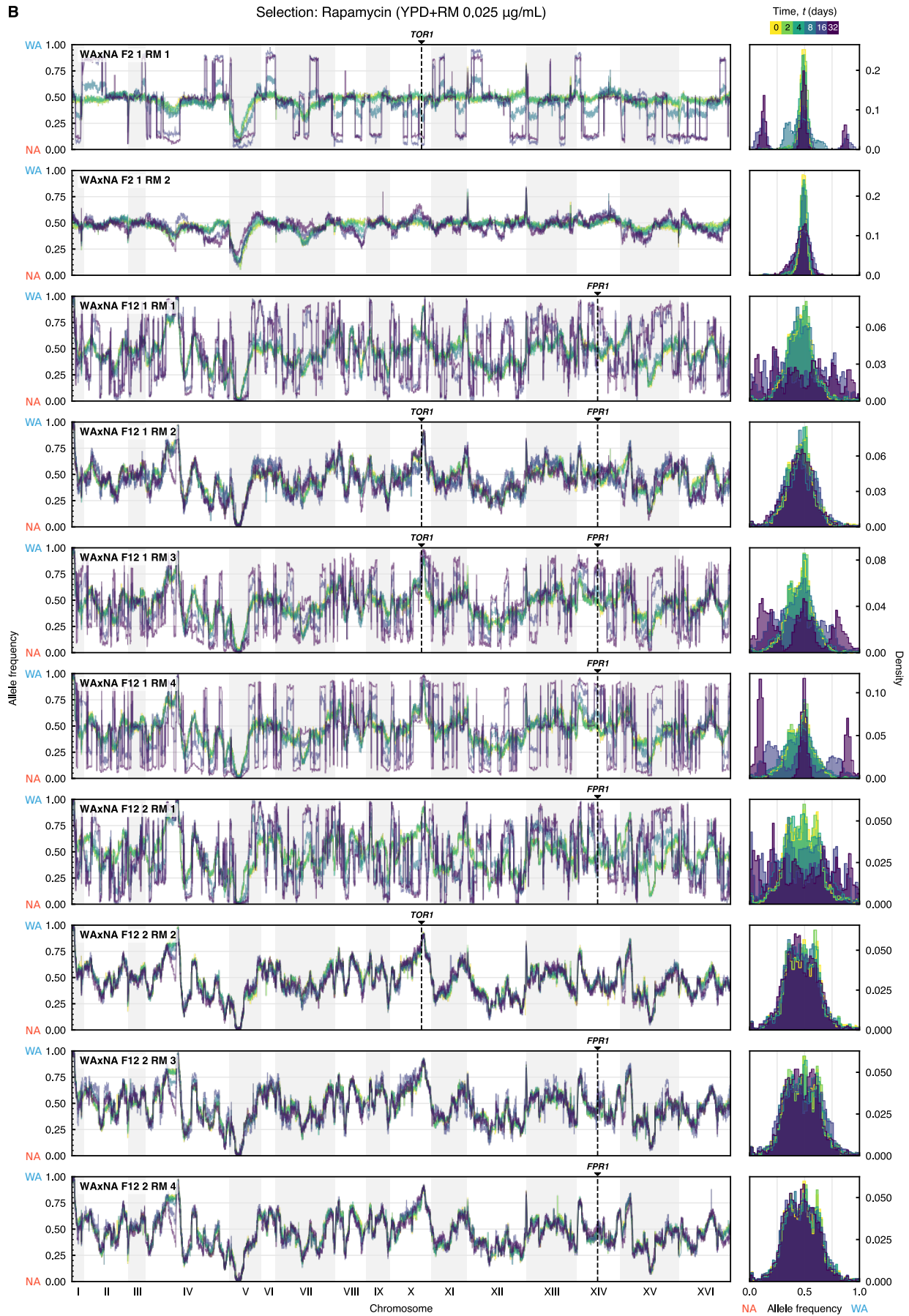
where  $\sigma_R^2$  is the variance contribution by random effects, any incremental fixed effect contributes additively to the fixed-effect variance, s.t.  $\sigma_F^2 = \text{Var}(\beta_t x_t + \beta_d x_d + \beta_x x_x)$ , and  $r^2$  represents the proportion of variance explained by the fixed and random effects combined. Dropping the  $\sigma_R^2$  term from the numerator, we can evaluate  $r^2$  and the fixed-effects variance  $r_F^2$  for linear mixed models, and estimate the background contribution to the variance by  $r^2 - r_F^2$ . Then to further assign the fixed-effect variances to individual variance components shown in Figure 6B, we used the simpler models and their estimated  $r_F^2$ . We note that modeling the background component using fixed effects instead leads to a variance decomposition that is nearly identical to the decomposition with linear mixed models described here. However, modeling the background as a fixed effect requires fitting a large number of parameters (one extra parameter per background) and thus describing the background by random effects is a better model for the data.

# Supplemental Figures



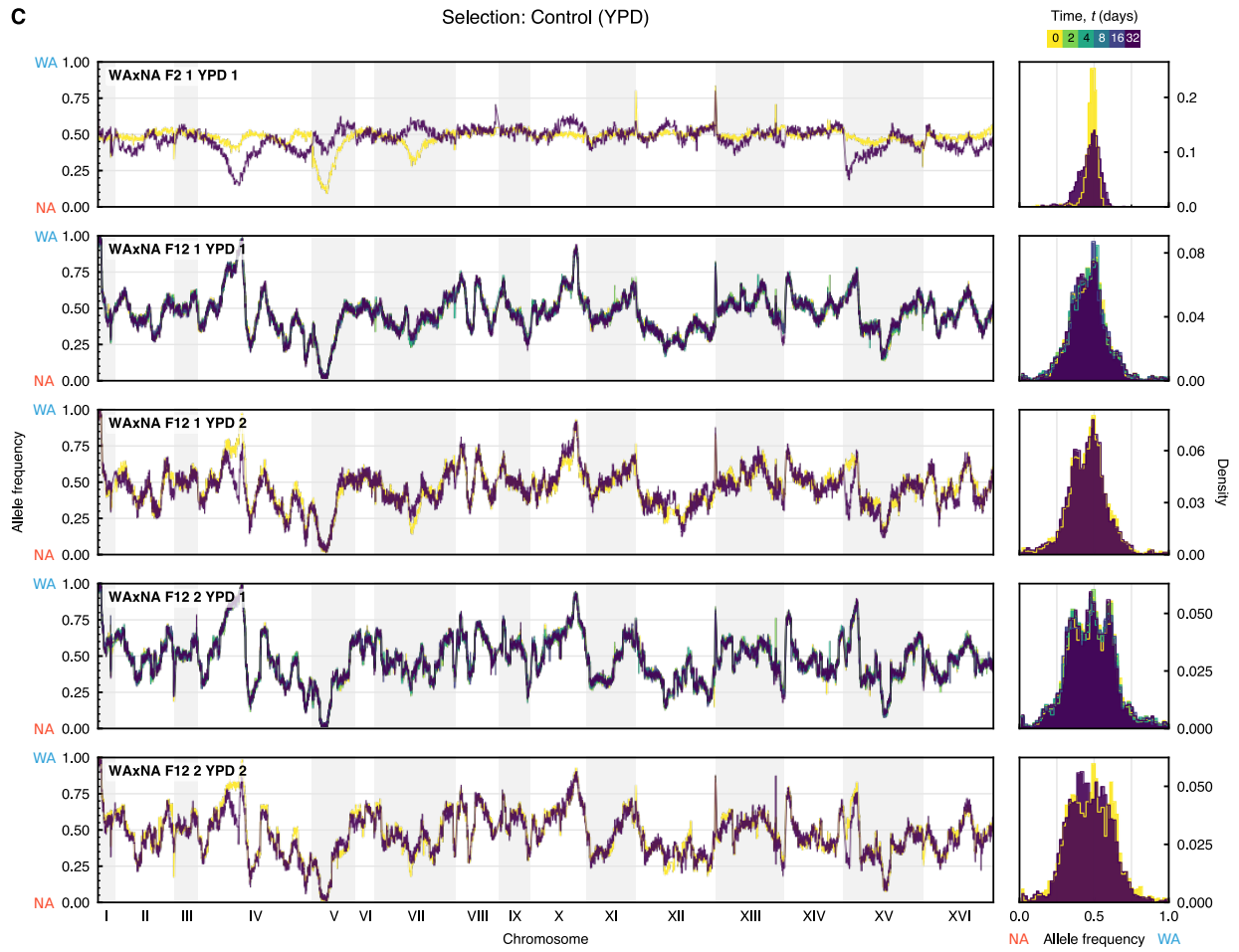
**Figure S1: Subclonal reconstruction of a simulated example. Related to Figures 2, 3A and 3C.** Subclonal reconstruction for a simulated example of two macroscopic subclones using cloneHD. The physical locations of the segregating sites are represented along the  $x$  axis and the  $y$  axis shows the allele frequency at every locus. **(A)** The true allele frequency of the bulk (grey) and the true genotypes  $g_{ij}$  of two subclones (blue and red) at locus  $j$  for the simulated example. **(B)** Simulated jumps (subclones) and diffusion (bulk), in the presence of two subclones of size  $f_j = (0.1, 0.0)$  at  $t_0$ ,  $f_j = (0.2, 0.1)$  at  $t_1$  and  $f_j = (0.6, 0.2)$  at  $t_2$ . The path along the genome is described by a mixture of the two, with jump probability  $p = 4 \times 10^{-5} \text{ bp}^{-1}$ , diffusion constant  $\sigma = 5 \times 10^{-4}$ , and binomial draws as emissions. The simulated observations are probabilistically color-coded according to the bulk fraction or each of the subclone fractions. The mean posterior estimate of the SNV emission in black solid line shows the accuracy of the reconstruction. The pie charts indicate the inferred bulk and subclone frequency estimates,  $\hat{f}_j$ .



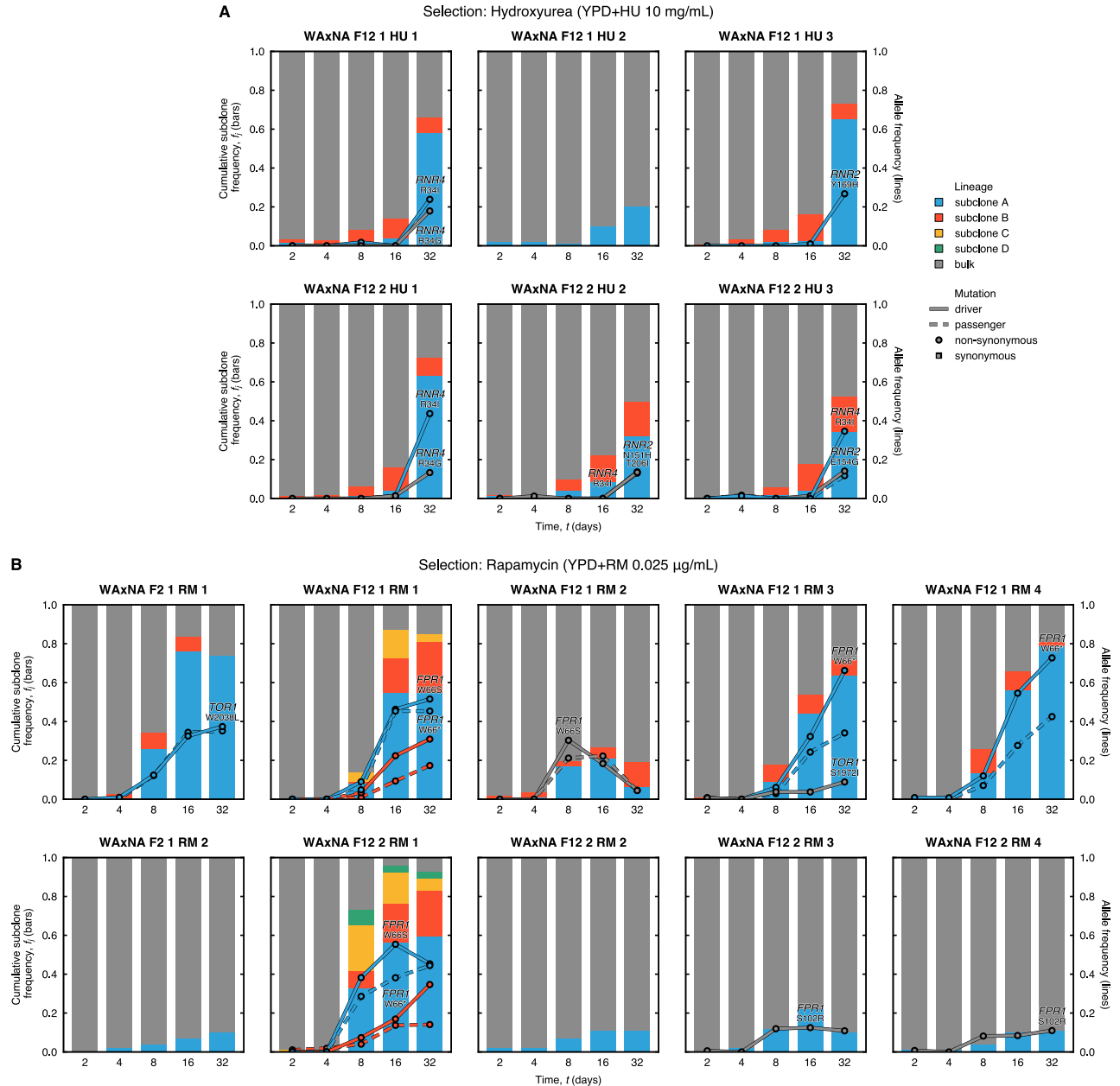


**Figure S2:** (continued)

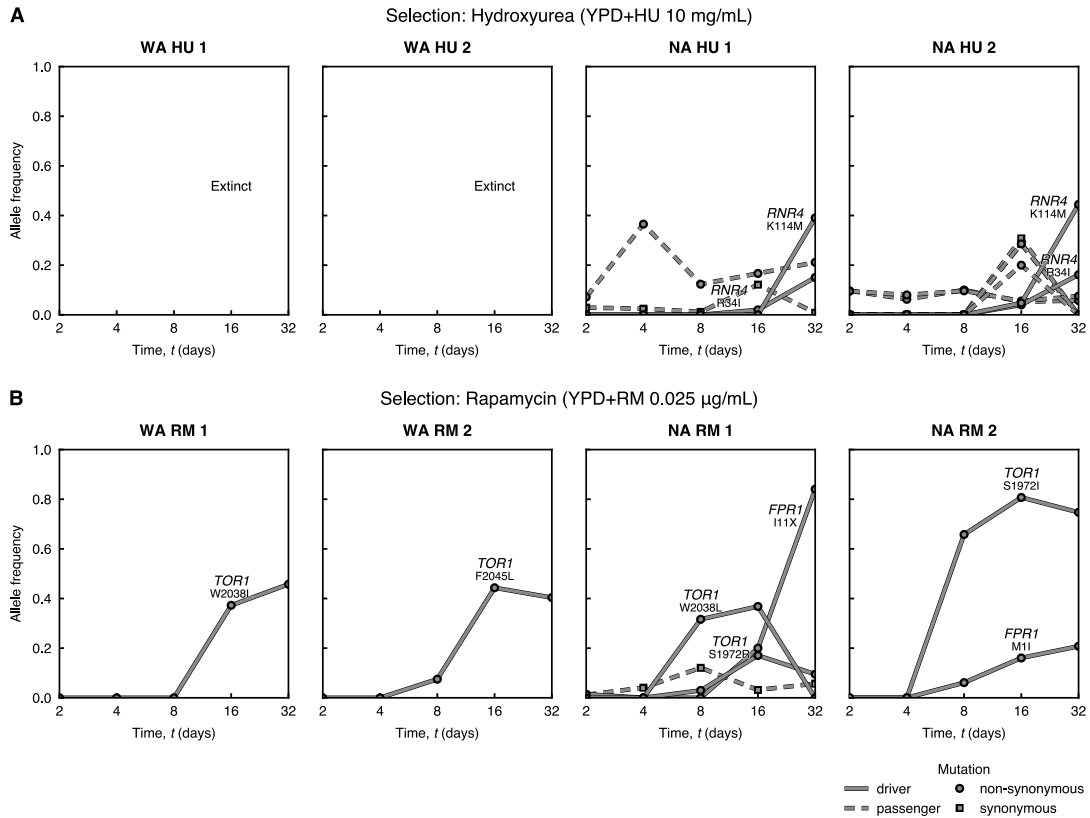




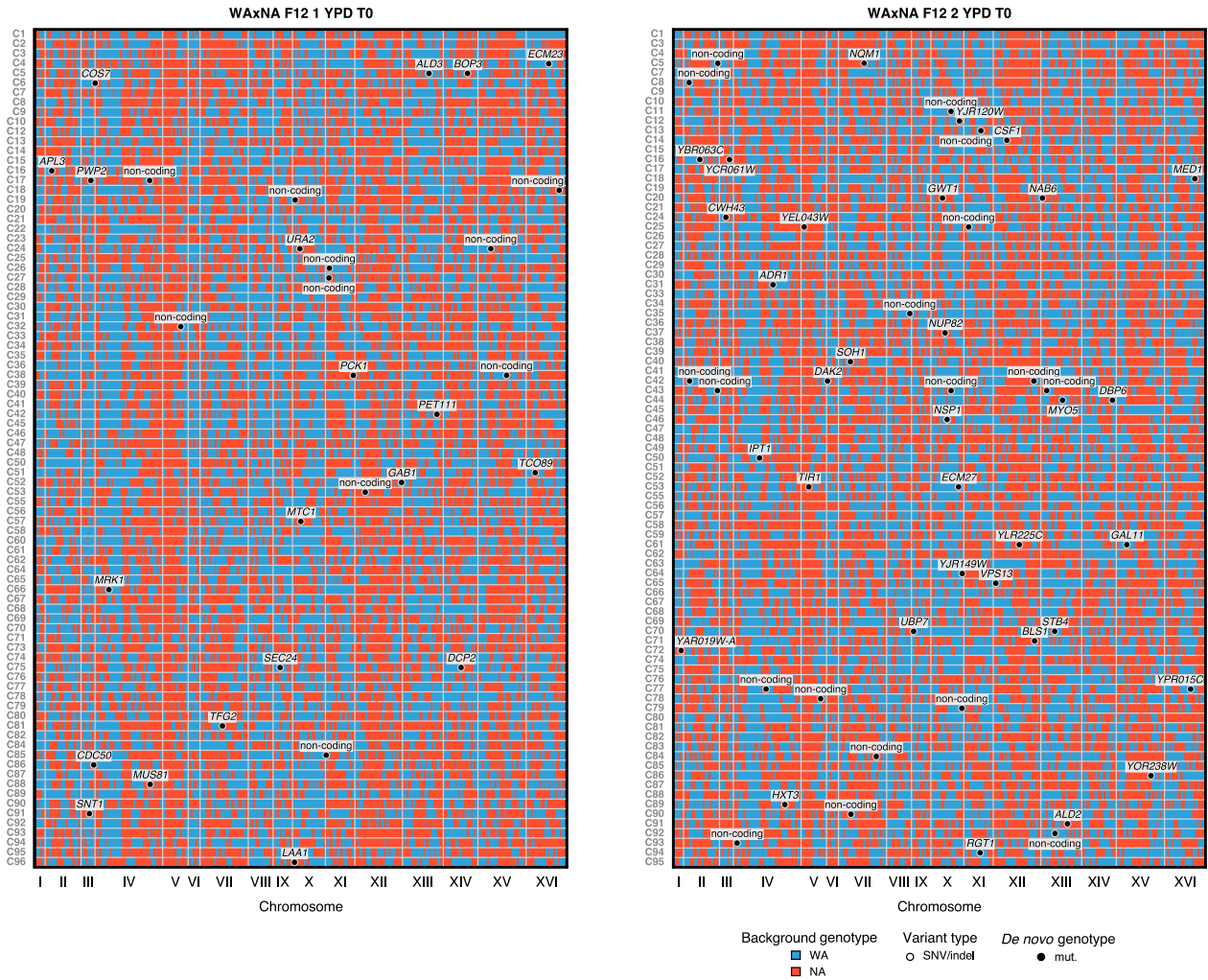
**Figure S2:** (continued)



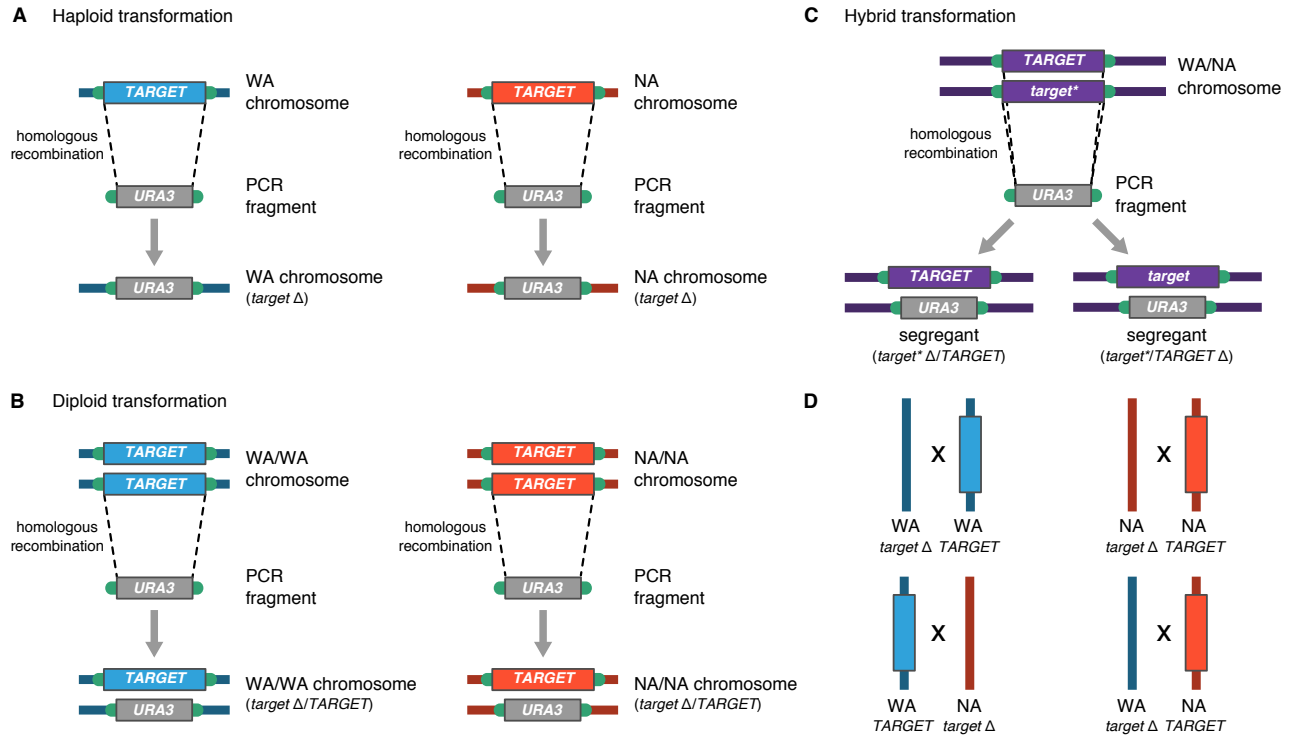
**Figure S3: Subclonal dynamics in WxNA populations. Related to Figures 3A and 3C.** Subclonal dynamics in time for WxNA founders evolved in (A) hydroxyurea and (B) rapamycin, measured by whole-population sequencing. Time is on the  $x$  axis, starting after crossing when the population has no competing subclones. Cumulative haplotype frequency of subclones (bars) and allele frequency of *de novo* mutants (lines) are on the  $y$  axis. The subclone frequencies are inferred from the frequency of pre-existing variants using cloneHD (see Figure S2). Driver mutations are solid lines and passenger mutations are dashed lines, colored by subclone assignment; circles and squares denote non-synonymous and synonymous mutations, respectively. For driver mutations, the mutated gene and codon are indicated above each line. No macroscopic subclones or *de novo* mutations were detected in any of the control replicates in YPD.



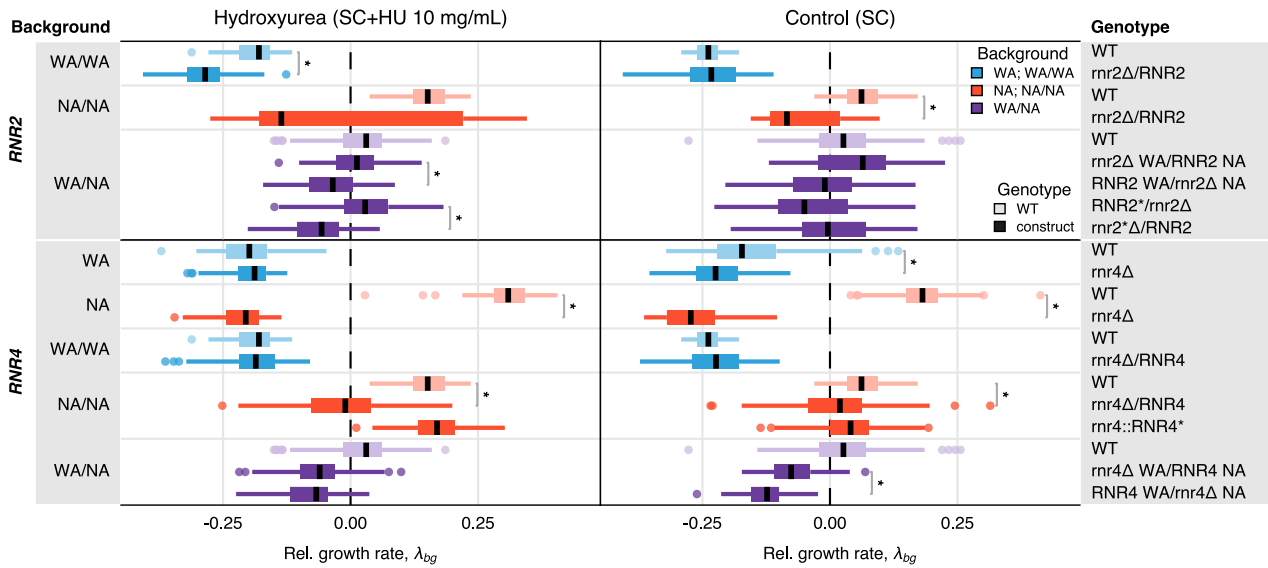
**Figure S4: Subclonal dynamics in WA and NA populations. Related to Figures 3A and 3C.** Subclonal dynamics in time for WA and NA founders evolved in (A) hydroxyurea and (B) rapamycin, measured by whole-population sequencing. WA founders evolved in hydroxyurea did not survive after  $t=4$  days. Driver mutations are solid lines and passenger mutations are dashed lines; circles and squares denote non-synonymous and synonymous mutations, respectively. For driver mutations, the mutated gene and codon are indicated above each line. No *de novo* mutations were detected in any of the control replicates in YPD.



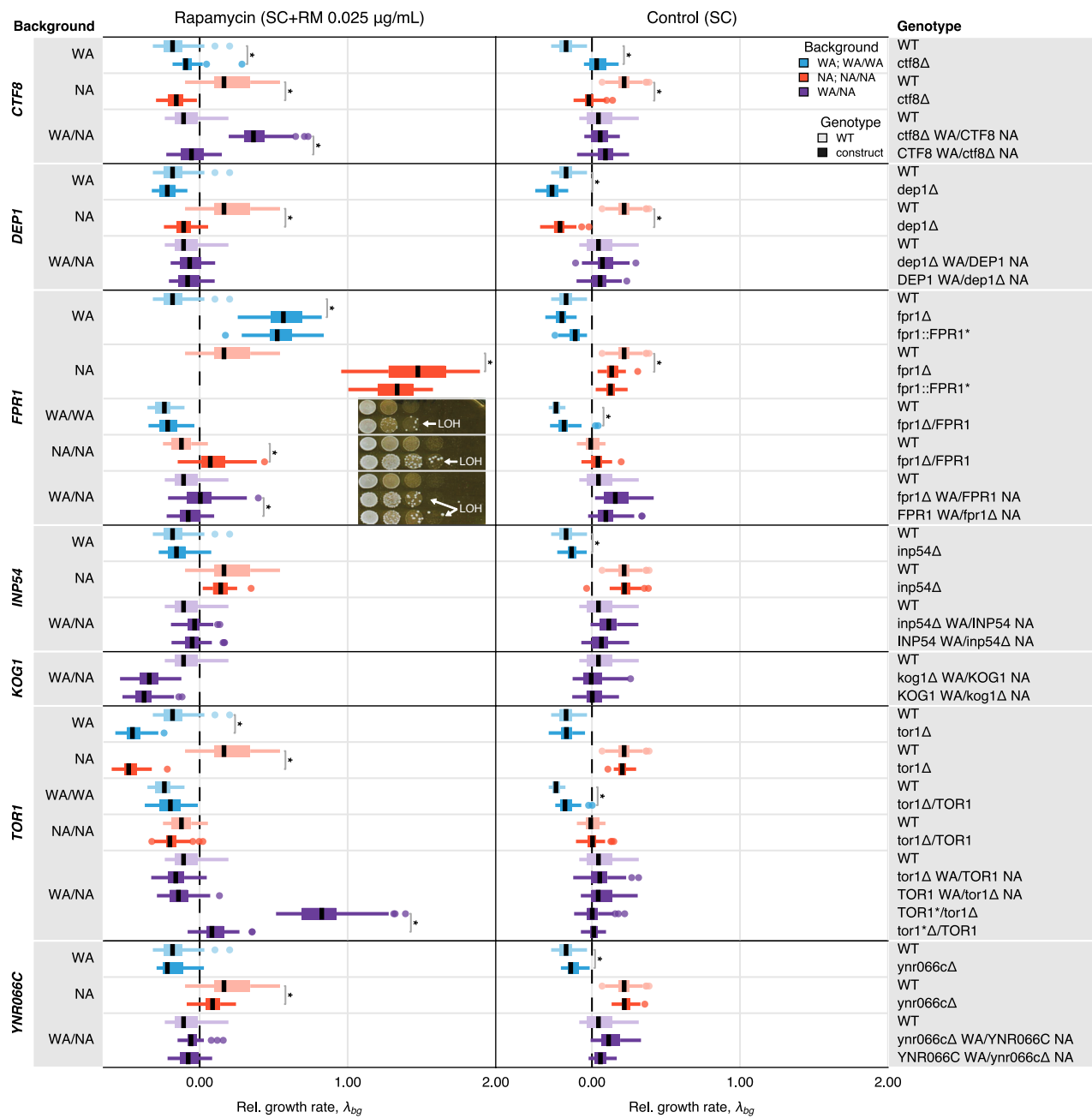
**Figure S5: Genetic heterogeneity in sequences of ancestral clonal isolates. Related to Figures 4 and 5A.** Whole-genome sequences of ancestral haploid clones sampled from the WAXNA F<sub>12</sub> founder populations, which were obtained by bulk crossing between the WA and NA parents. Pre-existing and *de novo* SNVs and indels were detected by whole-genome sequencing in single-cell clones derived from ancestral populations at  $t=0$  days. Chromosomes are shown on the  $x$  axis; clonal isolates are listed on the left. WA (in blue) and NA (in red) represent haploid genotypes of pre-existing variants. Individual cells with unique background genotypes carry private *de novo* SNVs and indels (circles). A copy-number gain of chromosome IX ( $n>2n$ ) was also found in clone C50 of WAXNA F<sub>12</sub> 2 YPD T0 (not shown).



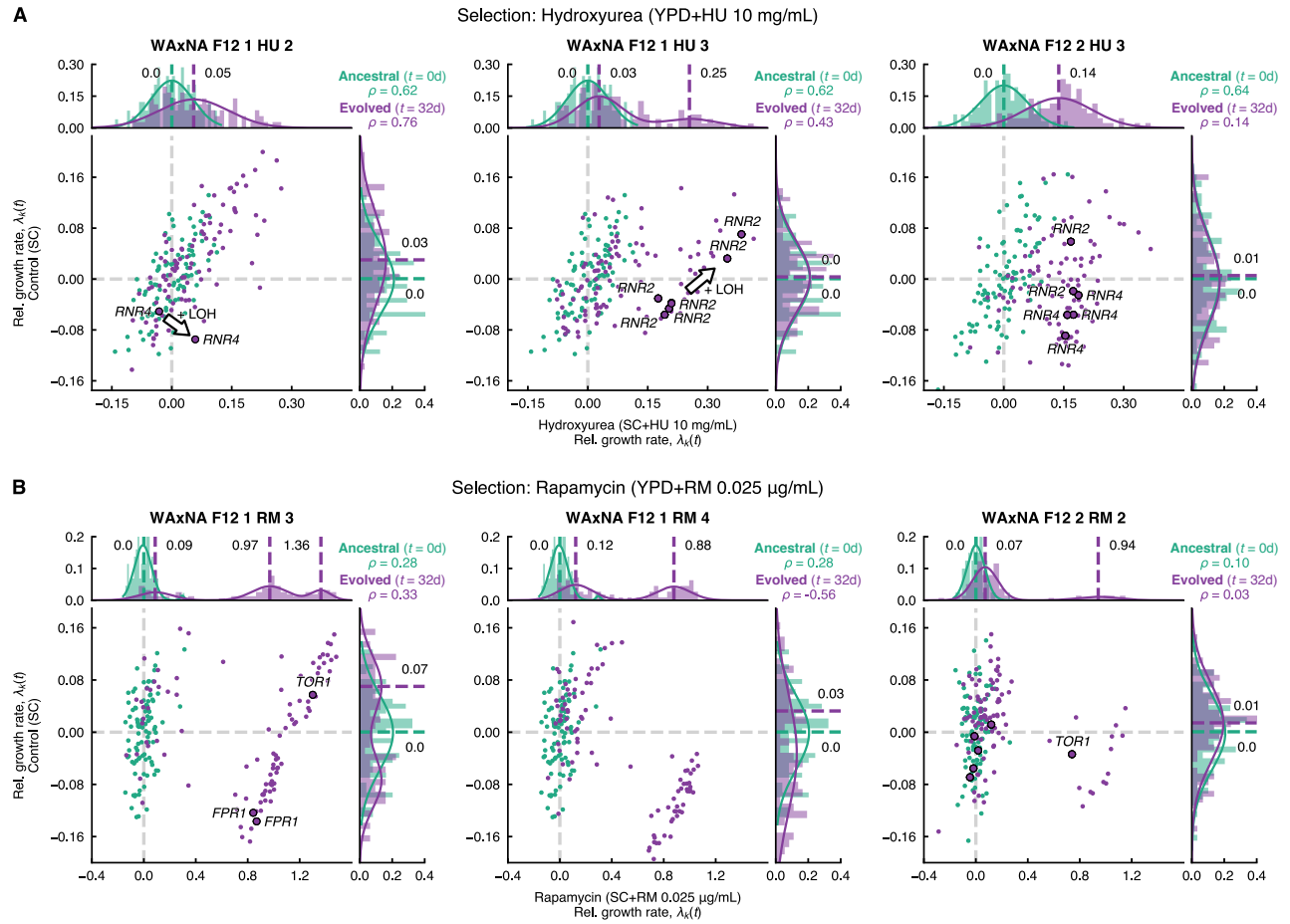
**Figure S6: Strategy for strain construction.** Gene deletions were mediated by homologous recombination between the terminals of the PCR product and the corresponding genomic sequence where the gene to be deleted ('target') is encoded. Blue and red lines indicate WA and NA chromosomes, respectively. Flanking regions in green indicate two different homologous sequences targeted for recombination, which are 30-40 bp long in *S. cerevisiae*. **(A)** Genes of interest were individually deleted in both WA and NA haploids, resulting in *rnr4*Δ, *fpr1*Δ and *tor1*Δ strains in both parental backgrounds. **(B)** A similar strategy was used to delete genes in WA and NA homozygous diploids. *RNR2* and *RNR4* were only deleted in one allele while there is the wild-type gene remaining in the other allele. **(C)** Evolved segregants with *de novo* mutations were isolated from the WAxNA F<sub>12</sub> populations. Using the same strategy, *RNR2* or *TOR1* mutants could be rid of either the wild-type allele or the mutated allele. The primer sequences used are listed in Supplemental Tables. **(D)** We crossed the strain constructed in (A) with the parental strain with wild-type gene, to obtain strains with deleted genes in WA, NA homozygous diploid and WA/NA hybrid.



**Figure S7: Validation tests for driver mutations in hydroxyurea.** Validation tests for driver mutations in hydroxyurea, measured in SC+HU (left panel) and SC (right panel). The relative growth rate,  $\lambda_{bg}$ , of each construct is shown for  $n_r = 64$  measurement replicates. Genetic constructs are grouped by candidate gene and by background of the construct, where the background  $b$  can be WA, NA (haploid); WA/WA, NA/NA (diploid); WA/NA (hybrid), and the genotype  $g$  can be wild-type for the gene, deleted or hemizygous. Relative growth rates are normalized with respect to the mean population growth rate  $\langle \lambda_k \rangle_{t=0}$  at  $t = 0$  days (see Figures 3B and S9A). Medians and 25%/75% percentiles are shown for each genetic construct, with medians as horizontal lines and outliers highlighted. The color of each of the boxes reflects the background (WA and WA/WA, blue; NA and NA/NA, red; WA/NA, purple). Lighter shades indicate a wild-type (WT) control for a specific background and darker shades are the candidate strains. For a given background, we compared deletion strains against their respective WT control (e.g. *rnr4* $\Delta$  vs WT in WA background) and hemizygous strains against the equivalent hemizygous strain where the opposite copy has been deleted (e.g. *rnr4* $\Delta$  WA/*RNR4* NA vs *RNR4* WA/*rnr4* $\Delta$  NA in WA/NA background). To test statistical significance we used a non-parametric Wilcoxon rank-sum test. Significance tests between two strains with  $p < 10^{-4}$  are highlighted with an asterisk.



**Figure S8: Validation tests for driver mutations in rapamycin. Related to Figure 2.** Validation tests for driver and passenger mutations in rapamycin, measured in SC+RM (left panel) and SC (right panel). The relative growth rate,  $\lambda_{bg}$ , of each construct is shown for  $n_r = 64$  measurement replicates. Genetic constructs are grouped by candidate gene and by background of the construct, where the background  $b$  can be WA, NA (haploid); WA/WA, NA/NA (diploid); WA/NA (hybrid), and the genotype  $g$  can be wild-type for the gene, deleted or hemizygous. Relative growth rates are normalized with respect to the mean population growth rate  $\langle \lambda_k \rangle_{t=0}$  at  $t = 0$  days (see Figures 3D and S9B). Medians and 25%/75% percentiles are shown for each genetic construct, with medians as horizontal lines and outliers highlighted. The color of each of the boxes reflects the background (WA and WA/WA, blue; NA and NA/NA, red; WA/NA, purple). Lighter shades indicate a wild-type (WT) control for a specific background and darker shades are the candidate strains. For a given background, we compared deletion strains against their respective WT control (e.g. *fpr1 $\Delta$*  vs WT in WA background) and hemizygous strains against the equivalent hemizygous strain where the opposite copy has been deleted (e.g. *fpr1 $\Delta$*  WA/*FPR1* NA vs *FPR1* WA/*fpr1 $\Delta$*  NA in WA/NA background). To test statistical significance we used a non-parametric Wilcoxon rank-sum test. Significance tests between two strains with  $p < 10^{-4}$  are highlighted with an asterisk. Visual inspection of *FPR1* heterozygous deletions using a spot assay (inset) manifests the immediate loss of the wild-type allele by LOH – validated by colony Sanger sequencing –.





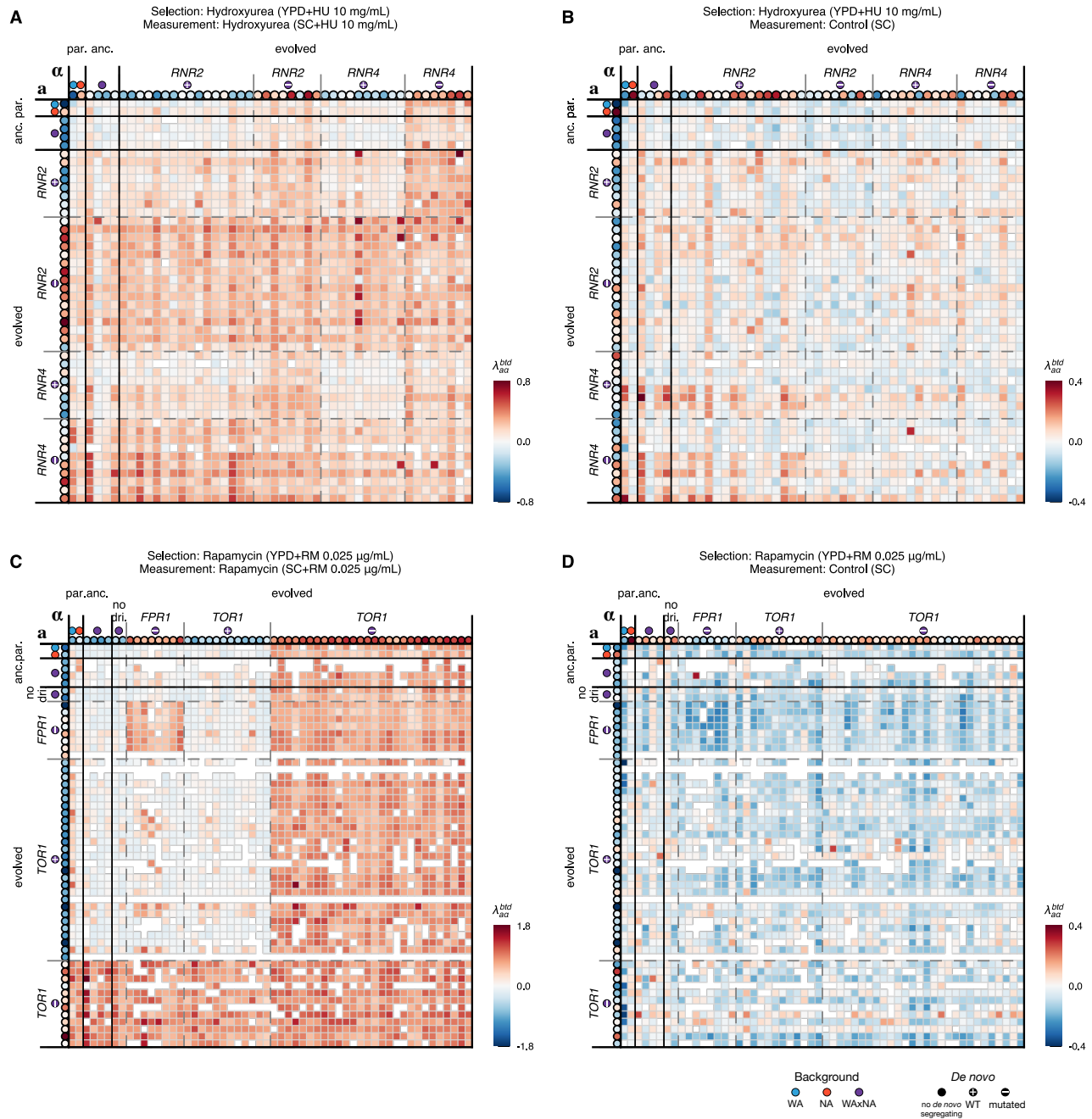


**Figure S10: Fitness contribution of genetic background and *de novo* mutations. Related to Figure 6.** Given an ensemble of  $n_b$  haploid spores with unique genetic backgrounds ( $n_b = 48$  in hydroxyurea and  $n_b = 56$  in rapamycin), every haploid spore is crossed against itself and all other haploid spores, and the two must be of opposite mating type (*MATa* or *MAT $\alpha$* ) to construct a matrix of diploid hybrids of size  $n_b \times n_b$ . In each panel, spores are represented along the vertical and horizontal axes of the matrix and hybrids are shown as matrix elements. Symbols follow the Figure 6A legend and indicate combinations of the type of genetic background (WA parent:  $\odot$ , NA parent:  $\ominus$ , WxNA segregant:  $\oplus$ ) and the genotype of *de novo* mutations (no *de novo* mutation:  $\bullet$ , wild-type:  $\oplus$ , mutated:  $\ominus$ ). Relative growth rates of spores  $\lambda_{\{a,\alpha\}}^{bid}$  and hybrids  $\lambda_{\alpha a}^{bid}$  are shown, normalized with respect to the ancestral WxNA cross. Each matrix element is labeled by background genotype  $b$ , *de novo* genotype  $d$ , and time of sampling during selection  $t$ . Measurements were taken in (A) SC+HU and (B) SC for populations selected in hydroxyurea; and (C) SC+RM and (D) SC for populations selected in rapamycin. The color scale for all matrices is shown to the right of each panel and indicates the growth rate difference with respect to the ancestral WxNA cross. White boxes indicate missing data due to mating inefficiency and slow growth.

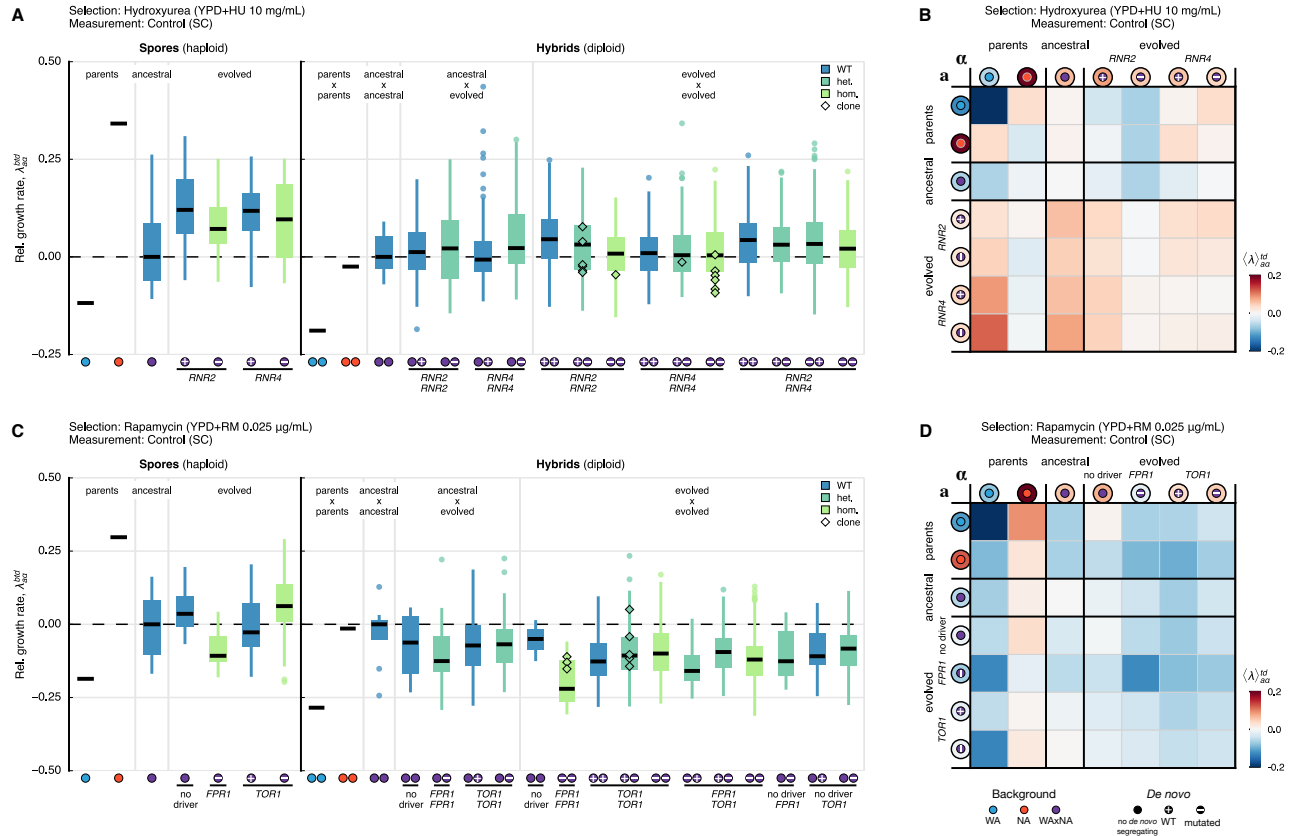


**Figure S11: Ensemble average of fitness effects over genetic backgrounds. Related to Figure 6.** To quantify the fitness effects of background variation and *de novo* mutations in the absence of stress, we measured the large recombinant library built with the genetic cross in a control environment (SC). Symbols follow the Figure 6A legend and indicate combinations of the type of genetic background (WA parent: ●, NA parent: ●, WAXNA segregant: ●) and the genotype of *de novo* mutations (no *de novo* mutation: ●, wild-type: ⊕, mutated: ⊖). (A and C) Relative growth rate of spores,  $\lambda_{a,\alpha}^{brd}$ , and hybrids,  $\lambda_{a,\alpha}^{brd}$ , measured for multiple combinations of background and *de novo* genotypes with respect to the ancestral population, and averaged over measurement replicates. Measurements were taken in (A) hydroxyurea and (C) rapamycin. Medians and 25%/75% percentiles across groups are shown, with medians as horizontal lines and colored by *de novo* genotype (wild-type, blue; heterozygote, cyan; homozygote, green). Outliers (circles) and isolated, selected clones with matching genotypes (diamonds) are highlighted. (B and D) Ensemble average of the relative growth rate of spores,  $\langle \lambda \rangle_{a,\alpha}^{td}$ , and hybrids,  $\langle \lambda \rangle_{a,\alpha}^{td}$ . Each matrix element is labeled by *de novo* genotype  $d$ , and time of sampling during selection  $t$ , and averaged over genetic backgrounds  $b$ . Measurements were taken in (B) hydroxyurea and (D) rapamycin. The color scale for all matrices is shown to the right of each panel and indicates the difference in the ensemble average with respect to the ancestral WAXNA cross.

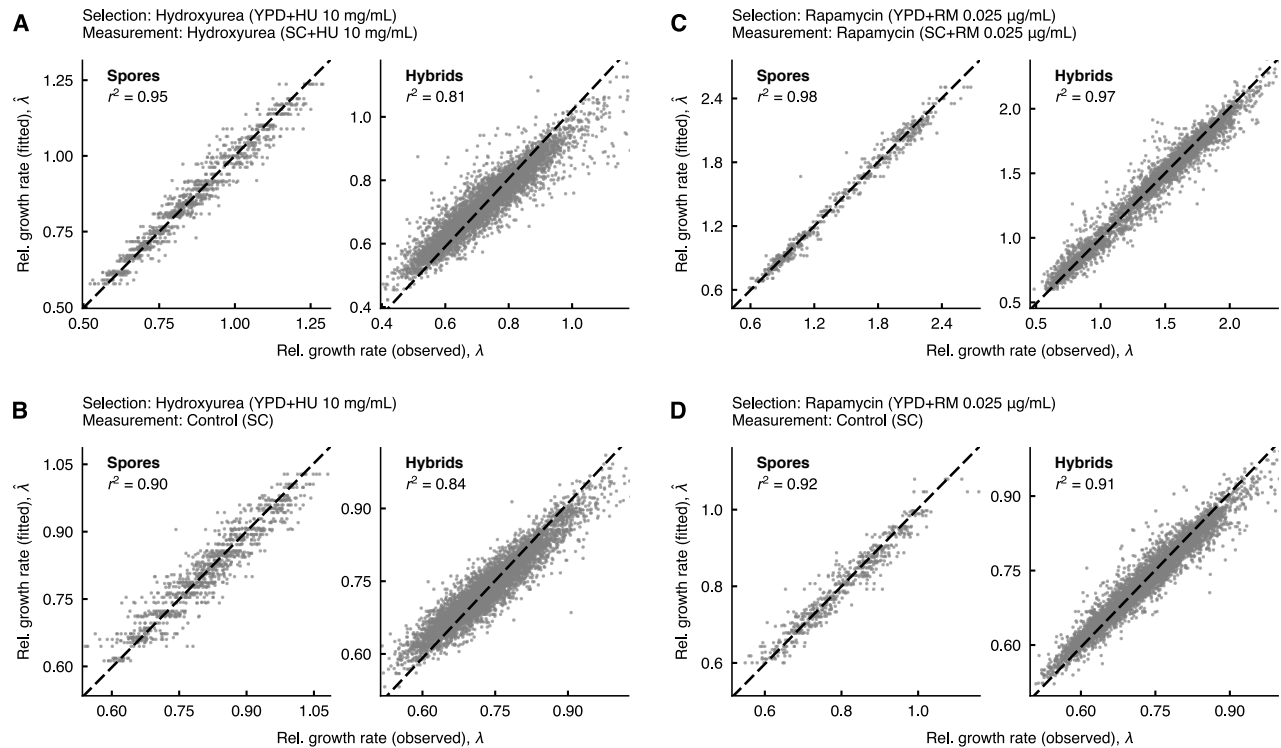


**Figure S12: Hierarchical analysis of variance in the genetic cross using a linear mixed model. Related to Figure 6.** We model the growth rate of spores,  $\lambda_{\{a,\alpha\}}^{bid}$ , and hybrids,  $\lambda_{aa}^{bid}$ , as a function of background genotype  $b$ , *de novo* genotype  $d$ , time of sampling during selection  $t$ , and auxotrophy  $x$ . Relative growth rates are accurately fitted by this model (Model 4). Model fits are summarized in Table S2. Measurements are taken in SC+HU and SC only for populations selected in hydroxyurea (**A** and **B**); and in SC+RM and SC only for populations selected in rapamycin (**C** and **D**). The scatter shows a set of measurements  $\lambda$  ( $x$  axis) against the fitted rates  $\hat{\lambda}$  ( $y$  axis). The total variance explained,  $r^2$ , is separately computed for spores and hybrids by environment.

# Supplemental Tables

**Table S1: Populations and clonal isolates analyzed by whole-genome sequencing. Related to Table 1.** Summary of populations and clonal isolates analyzed by whole-genome sequencing in this study. The best-fit number of subclones  $N_c$  as estimated by cloneHD are shown together with the total clonal fraction,  $F^t = \sum_{j=1}^n f_j^t$ , after 32 days of selection. Per population, the union set of driver mutations found by whole-population and clone genome sequencing is shown. The genotypes of driver mutations found in clonal isolates were validated by Sanger sequencing (labeled by §). WA/WA populations in hydroxyurea did not survive beyond 4 days of selection (labeled by †).

Time	Background	Cross		Selection			Clonality		Drivers		
		Gen.	Rep.	Environment	Rep.	Isolates	$N_c$	$F^t$			
0 days	WA/WA	–	–	YPD	–	–	–	–			
	NA/NA	–	–	YPD	–	–	–	–			
	WAxNA	F <sub>12</sub>	1	YPD	–	C1–C96	–	–			
2–32 days	WA/WA	–	–	YPD+HU	1 <sup>†</sup>	–	–	–			
					2 <sup>†</sup>	–	–	–			
				YPD+RM	1	–	–	–	<i>TOR1</i> W2038L <sup>§</sup>		
					2	–	–	–	<i>TOR1</i> F2045L <sup>§</sup>		
					2	–	–	–	<i>RNR4</i> R34I <sup>§</sup> , K114M <sup>§</sup>		
					2	–	–	–	<i>RNR4</i> R34I <sup>§</sup> , K114M <sup>§</sup>		
	NA/NA	–	–	YPD+HU	1	–	–	–	<i>RNR4</i> R34I <sup>§</sup> , K114M <sup>§</sup>		
					2	–	–	–	<i>RNR4</i> R34I <sup>§</sup> , K114M <sup>§</sup>		
				YPD+RM	1	–	–	–	<i>FPR1</i> K11fs <sup>§</sup> ; <i>TOR1</i> S1972R, W2038L <sup>§</sup>		
					2	–	–	–	<i>FPR1</i> M11 <sup>§</sup> ; <i>TOR1</i> S1972I <sup>§</sup>		
					2	–	–	–	<i>TOR1</i> W2038L		
					2	–	–	–			
	WAxNA	F <sub>2</sub>	1	YPD+RM	1	–	2	0.74	<i>TOR1</i> W2038L		
					2	–	1	0.10			
					1	–	0	–			
		F <sub>12</sub>	1	YPD	1	–	0	–			
				YPD+HU	1	C1–C2	2	0.58	<i>RNR4</i> R34G <sup>§</sup> , R34I <sup>§</sup>		
					2	C1–C2	1	0.20	<i>RNR4</i> R34I <sup>§</sup>		
					3	C1–C6	2	0.65	<i>RNR2</i> Y169H <sup>§</sup> ; chr. II LOH		
				YPD+RM	1	C1–C3	3	0.85	<i>CTF8</i> <sup>NA</sup> ; <i>FPR1</i> W66* <sup>§</sup> , W66S		
					2	C1–C6	2	0.20	<i>CTF8</i> <sup>NA</sup> ; <i>FPR1</i> W66S; <i>TOR1</i> W2038L <sup>§</sup>		
					3	C1–C3	2	0.72	<i>CTF8</i> <sup>NA</sup> ; <i>FPR1</i> W66* <sup>§</sup> ; <i>TOR1</i> S1972I		
					4	–	2	0.81	<i>CTF8</i> <sup>NA</sup> ; <i>FPR1</i> W66* <sup>§</sup>		
				YPD	1	–	0	–			
					2	–	0	–			
					2	YPD+HU	1	C1–C2	2	0.63	<i>RNR4</i> R34G <sup>§</sup> , R34I <sup>§</sup>
					2		2	C1–C4	2	0.32	<i>RNR2</i> N151H, T206I <sup>§</sup> ; <i>RNR4</i> R34I <sup>§</sup>
	3		2	C1–C6	2	0.34	<i>RNR2</i> E154G <sup>§</sup> ; <i>RNR4</i> R34I <sup>§</sup>				
YPD+RM	1	C1–C3	4	0.93	<i>CTF8</i> <sup>NA</sup> ; <i>FPR1</i> W66S, W66* <sup>§</sup>						
	2	C1–C6	1	0.10	<i>CTF8</i> <sup>NA</sup> ; <i>TOR1</i> W2038C <sup>§</sup>						
	3	C1	1	0.10	<i>CTF8</i> <sup>NA</sup> ; <i>FPR1</i> S102R						
	4	–	1	0.11	<i>CTF8</i> <sup>NA</sup> ; <i>FPR1</i> S102R						
YPD	1	–	0	–							
	2	–	0	–							

**Table S2: Statistical support for variance components in the genetic cross estimated using linear mixed models. Related to Figure 6B.** Summary statistics for linear mixed models of the genetic cross, fitted using restricted maximum likelihood. Models were separately fitted for spores and hybrids in each environment. The number of unique backgrounds  $n_b$  is much greater than the number of degrees of freedom (d.o.f.) for the parameters being fitted. Each background  $b$  was measured in several technical replicates. We selected the best model by maximum AIC (labeled by §). The breakdown of variance components in Model 4 is shown in Figure 6B and the models fits to the data are shown in Figure S12.

Selection	Measurement	Type	Model	d.o.f.	Variance		Log-likelihood	AIC	
					$r_F^2$	$r^2$			
Hydroxyurea (YPD+HU)	Hydroxyurea (SC+HU)	Spores $n_b = 92$	1	3	0.0000	0.9500	1813.367	-3627.063	
			2	4	0.1071	0.9504	1816.932	-3636.219	
			3§	7	0.5338	0.9507	1841.920	-3697.223	
			4	8	0.5338	0.9509	1839.372	-3695.832	
		Hybrids $n_b = 2013$	1	3	0.0000	0.8045	6535.699	-13075.484	
			2	5	0.0652	0.8044	6608.318	-13230.265	
	Hydroxyurea (YPD+HU)	Control (SC)	Spores $n_b = 92$	1	3	0.0000	0.8914	1918.357	-3837.994
				2	4	0.0381	0.8924	1917.974	-3840.051
				3	7	0.0605	0.8954	1911.224	-3836.707
				4§	8	0.1559	0.8957	1913.807	-3846.480
			Hybrids $n_b = 2013$	1	3	0.0000	0.8335	9435.532	-18875.965
				2	5	0.0009	0.8337	9429.119	-18874.079
Rapamycin (YPD+RM)	Rapamycin (SC+RM)	Spores $n_b = 104$	1	3	0.0000	0.9815	438.848	-875.752	
			2	4	0.0924	0.9817	443.237	-884.134	
			3	7	0.8146	0.9815	524.504	-1054.421	
			4§	8	0.8699	0.9815	542.282	-1094.737	
		Hybrids $n_b = 2271$	1	3	0.0000	0.9583	2368.301	-4738.294	
			2	5	0.0355	0.9584	2407.246	-4819.913	
	Rapamycin (YPD+RM)	Control (SC)	Spores $n_b = 104$	3	17	0.7422	0.9675	4465.029	-8981.497
				4§	18	0.7430	0.9675	4466.273	-8987.264
				1	3	0.0000	0.9217	1038.794	-2078.815
				2	4	0.0011	0.9224	1036.569	-2076.940
			Hybrids $n_b = 2270$	3	7	0.1711	0.9239	1039.674	-2092.692
				4§	8	0.3953	0.9235	1054.494	-2128.413
Rapamycin (YPD+RM)	Control (SC)	Spores $n_b = 104$	1	3	0.0000	0.9065	11394.150	-22793.196	
			2	5	0.0173	0.9066	11408.580	-22832.161	
			3	17	0.0593	0.9072	11418.030	-22915.694	
			4§	18	0.0697	0.9071	11428.480	-22941.867	
		Hybrids $n_b = 2270$	1	3	0.0000	0.9065	11394.150	-22793.196	
			2	5	0.0173	0.9066	11408.580	-22832.161	

**Glossary of wild strains used in this study, including derivative strains.** \*Isolated in West Africa (pre-1914) by A. Guil-  
liermond from bili wine from *Osbeckia grandiflora* (Liti et al., 2009). †Isolated in Pennsylvania (1999) by P. Sniegowski  
from soil beneath *Quercus alba* (Sniegowski et al., 2002).

Background	ID	Derived from	Genotype
WA	DBVPG6044	Wild isolate*	
	CC402	DBVPG6044	<i>MATa, ura3::KanMX, ho::HygMX</i>
	CC406	DBVPG6044	<i>MATα, ura3::KanMX, lys2::URA3, ho::HygMX</i>
	FS174	DBVPG6044	<i>MATα, ura3::KanMX, ho::NatMX</i>
	YGL1001	DBVPG6044	<i>MATa/α, ura3Δ0; ura3Δ0; leu2Δ0; leu2Δ0; lys2Δ0; met15Δ0</i>
WA/WA	CC426	CC402 × CC406	<i>MATa/α, ura3::KanMX/ura3::KanMX, ho::HygMX/ho::HygMX, LYS2/lys2::URA3</i>
NA	YPS128	Wild isolate†	
	CC403	YPS128	<i>MATa, ura3::KanMX, ho::HygMX</i>
	CC407	YPS128	<i>MATα, ura3::KanMX, lys2::URA3, ho::HygMX</i>
	FS173	YPS128	<i>MATα, ura3::KanMX, ho::NatMX</i>
	YGL1011	YPS128	<i>MATa/α, ura3Δ0; ura3Δ0; leu2Δ0; leu2Δ0; lys2Δ0; met15Δ0</i>
NA/NA	CC440	CC403 × CC407	<i>MATa/α, ura3::KanMX/ura3::KanMX, ho::HygMX/ho::HygMX, LYS2/lys2::URA3</i>
WA/NA	CC427	CC402 × CC407	<i>MATa/α, ura3::KanMX/ura3::KanMX, ho::HygMX/ho::HygMX, LYS2/lys2::URA3</i>
	CC435	CC403 × CC406	<i>MATa/α, ura3::KanMX/ura3::KanMX, ho::HygMX/ho::HygMX, LYS2/lys2::URA3</i>

**Glossary of strains with genetic constructs used in this study.** The genetic constructs are grouped by the ‘target’ gene of interest and are engineered in multiple genetic backgrounds. They include gene deletions, hemizygous constructs of ancestral alleles (WA and NA) and hemizygous constructs of evolved alleles.

Gene	ID	Derived from	Genotype
<i>CTF8</i>	YGL1269	DBVPG6044	<i>MATa, ho::HygMX, ura3::KanMX, ctf8::URA3</i>
	YGL1270	YPS128	<i>MATa, ho::HygMX, ura3::KanMX, ctf8::URA3</i>
	YGL1271	DBVPG6044 × YPS128	<i>MATa/α, ho::HygMX, ho::NatMX, ura3::KanMX, CTF8(NA)/ctf8(wa)::URA3</i>
	YGL1272	DBVPG6044 × YPS128	<i>MATa/α, ho::HygMX, ho::NatMX, ura3::KanMX, CTF8(WA)/ctf8(na)::URA3</i>
<i>DEP1</i>	YGL1562	DBVPG6044	<i>MATa, ho::HygMX, ura3::KanMX, dep1::URA3</i>
	YGL1563	YPS128	<i>MATa, ho::HygMX, ura3::KanMX, dep1::URA3</i>
	YGL1570	DBVPG6044 × YPS128	<i>MATa/α, ho::HygMX, ho::NatMX, ura3::KanMX, DEP1(NA)/dep1(wa)::URA3</i>
	YGL1571	DBVPG6044 × YPS128	<i>MATa/α, ho::HygMX, ho::NatMX, ura3::KanMX, DEP1(WA)/dep1(na)::URA3</i>
<i>FPR1</i>	YGL2166	CC402	<i>MATa, ura3::KanMX, ho::HygMX, fpr1::URA3</i>
	YGL2167	CC403	<i>MATa, ura3::KanMX, ho::HygMX, fpr1::URA3</i>
	YGL2181	FS174 × YGL2166	<i>MATa/α, ura3::KANMX/ura3::KANMX, ho::HYGMX/ho::NATMX, fpr1::URA3/FPR1</i>
	YGL2182	FS173 × YGL2167	<i>MATa/α, ura3::KANMX/ura3::KANMX, ho::HYGMX/ho::NATMX, fpr1::URA3/FPR1</i>
	YGL2184	FS173 × YGL2166	<i>MATa/α, ura3::KANMX/ura3::KANMX, ho::HYGMX/ho::NATMX, fpr1(wa)::URA3/FPR1(NA)</i>
	YGL2183	FS174 × YGL2167	<i>MATa/α, ura3::KANMX/ura3::KANMX, ho::HYGMX/ho::NATMX, fpr1(na)::URA3/FPR1(WA)</i>
	YGL2175	YGL2166	<i>MATa, ura3::KanMX, ho::HygMX, fpr1::FPR1*</i>
	YGL2193	YGL2167	<i>MATa, ura3::KANMX, ho::HYGMX, fpr1::FPR1*</i>
<i>INP54</i>	YGL1564	DBVPG6044	<i>MATa, ho::HygMX, ura3::KanMX, inp54::URA3</i>
	YGL1565	YPS128	<i>MATa, ho::HygMX, ura3::KanMX, inp54::URA3</i>
	YGL1572	DBVPG6044 × YPS128	<i>MATa/α, ho::HygMX, ho::NatMX, ura3::KanMX, INP54(NA)/inp54(wa)::URA3</i>
	YGL1573	DBVPG6044 × YPS128	<i>MATa/α, ho::HygMX, ho::NatMX, ura3::KanMX, INP54(WA)/inp54(na)::URA3</i>
<i>KOG1</i>	YGL1264	DBVPG6044 × YPS128	<i>MATa/α, ho::HygMX, ho::NatMX, ura3::KanMX, KOG1(NA)/kog1(wa)::URA3</i>
	YGL1263	DBVPG6044 × YPS128	<i>MATa/α, ho::HygMX, ho::NatMX, ura3::KanMX, KOG1(WA)/kog1(na)::URA3</i>
<i>RNR2</i>	YGL2164	DBVPG6044	<i>MATa/α, ura3Δ0, ura3Δ0, leu2Δ0, leu2Δ0, lys2Δ0, met15Δ0, RNR2/rnr2::URA3</i>
	YGL2165	YPS128	<i>MATa/α, ura3Δ0, ura3Δ0, leu2Δ0, leu2Δ0, lys2Δ0, met15Δ0, RNR2/rnr2::URA3</i>
	YGL2391	CC427	<i>MATa/α, ura3::KanMX/ura3::KanMX, ho::HygMX/ho::HygMX, LYS2/lys2::URA3, RNR2(NA)/rnr2(wa)::NATMX</i>
	YGL2392	CC427	<i>MATa/α, ura3::KanMX/ura3::KanMX, ho::HygMX/ho::HygMX, LYS2/lys2::URA3, RNR2(WA)/rnr2(na)::NATMX</i>
<i>RNR4</i>	YGL2198	WAXNA F12 2 HU 2 T32 C2	<i>MATa/α, ura3::KanMX/ura3::KanMX, LYS2/lys2::URA3, rnr2::NATMX/RNR2</i>
	YGL2189	WAXNA F12 2 HU 2 T32 C2	<i>MATa/α, ura3::KanMX/ura3::KanMX, LYS2/lys2::URA3, rnr2*/RNR2::NATMX</i>
	YGL2174	CC402	<i>MATa, ura3::KanMX, ho::HygMX, rnr4::URA3, aneuploidy in chr. VII (w/ RNR4)</i>
	YGL2170	CC403	<i>MATa, ura3::KanMX, ho::HygMX, rnr4::URA3</i>
	YGL2177	FS174 × YGL2174	<i>MATa/α, ura3::KANMX/ura3::KANMX, ho::HYGMX/ho::NATMX, rnr4::URA3/RNR4</i>
	YGL2178	FS173 × YGL2170	<i>MATa/α, ura3::KANMX/ura3::KANMX, ho::HYGMX/ho::NATMX, rnr4::URA3/RNR4</i>
	YGL2180	FS173 × YGL2174	<i>MATa/α, ura3::KANMX/ura3::KANMX, ho::HYGMX/ho::NATMX, rnr4::URA3/RNR4</i>
	YGL2179	FS174 × YGL2170	<i>MATa/α, ura3::KANMX/ura3::KANMX, ho::HYGMX/ho::NATMX, rnr4::URA3/RNR4</i>
<i>TOR1</i>	YGL2194	YGL1001	<i>MATa/α, ura3Δ0; ura3Δ0; leu2Δ0; leu2Δ0; lys2Δ0; met15Δ0; RNR4(WA)/rnr4(wa)::URA3</i>
	YGL2196	YGL1011	<i>MATa/α, ura3Δ0; ura3Δ0; leu2Δ0; leu2Δ0; lys2Δ0; met15Δ0; RNR4(NA)/rnr4(na)::URA3</i>
	YGL2176	YGL2170	<i>MATa, ura3::KanMX, ho::HygMX, rnr4::RNR4*</i>
	YGL2168	CC402	<i>MATa, ura3::KanMX, ho::HygMX, tor1::URA3</i>
	YGL2169	CC403	<i>MATa, ura3::KanMX, ho::HygMX, tor1::URA3</i>
	YGL2185	FS174 × YGL2168	<i>MATa/α, ura3::KANMX/ura3::KANMX, ho::HYGMX/ho::NATMX, tor1::URA3/TOR1</i>
	YGL2186	FS173 × YGL2169	<i>MATa/α, ura3::KANMX/ura3::KANMX, ho::HYGMX/ho::NATMX, tor1::URA3/TOR1</i>
	YGL2188	FS173 × YGL2168	<i>MATa/α, ura3::KANMX/ura3::KANMX, ho::HYGMX/ho::NATMX, tor1(wa)::URA3/TOR1(NA)</i>
<i>YNR066C</i>	YGL2187	FS174 × YGL2169	<i>MATa/α, ura3::KANMX/ura3::KANMX, ho::HYGMX/ho::NATMX, tor1(na)::URA3/TOR1(WA)</i>
	YGL2201	WAXNA F12 2 RM 2 T32 C6	<i>MATa/α, ura3::KanMX/ura3::KanMX, LYS2/lys2::URA3, tor1::NATMX/TOR1</i>
	YGL2191	WAXNA F12 2 RM 2 T32 C6	<i>MATa/α, ura3::KanMX/ura3::KanMX, LYS2/lys2::URA3, tor1*/TOR1::NATMX</i>
	YGL1566	DBVPG6044	<i>MATa, ho::HygMX, ura3::KanMX, ynr066c::URA3</i>
	YGL1567	YPS128	<i>MATa, ho::HygMX, ura3::KanMX, ynr066c::URA3</i>
	YGL1574	DBVPG6044 × YPS128	<i>MATa/α, ho::HygMX, ho::NatMX, ura3::KanMX, YNR066C/ynr066c::URA3</i>
	YGL1575	DBVPG6044 × YPS128	<i>MATa/α, ho::HygMX, ho::NatMX, ura3::KanMX, YNR066C/ynr066c::URA3</i>

**Primers for amplification of putative drivers.** Sequence of primers used to amplify the genes containing putative driver mutations.

Gene	Orientation	Chr	Target		Sequence (TARGET)
			Start	End	
<i>DEP1</i>	fwd	I	128977	128996	CAGAGAGCTGGTCCAGTTCA
	rev	I	129573	129554	TGGCCTCATCTATCGCCTCT
<i>FPR1</i>	fwd	XIV	371600	371619	CCCTCCTGCCACAAGAGTTT
	rev	XIV	372170	372151	TGCCACCTTCCCAAAGACAG
<i>INP54</i>	fwd	XV	205005	205024	GCGAAAGTTGGCACTGCATA
	rev	XV	205624	205605	GCTACACAAGGGGATGAGCA
<i>RNR2</i>	fwd	X	392707	392726	CGTGCCGAAGCTTCTTCTG
	rev	X	393245	393226	CATGCAAAGTCGGTGTGCAA
<i>RNR4</i>	fwd	VII	855968	855987	CAGGGTTTTGCAATTGGGCA
	rev	VII	856843	856824	TACGACCACCCAACACCAAG
<i>TOR1</i>	fwd	X	565069	565088	AGCCAGATCCTACGGTGAGT
	rev	X	565652	565633	CCCAGGAACAGCCAATTCGA
<i>YNR066C</i>	fwd	XIV	753660	753679	TCGAATTCCTACCGTCGCC
	rev	XIV	754369	754348	GCCGCATATACACAATTAGCCT



**Primers used to engineer genetic constructs.** Sequence of primers used to engineer gene deletions (see ‘Engineered genetic constructs’).

Gene	Marker	Orientation	Chr	Target		Sequence (TARGET, <i>ura3/natMX</i> )
				Start	End	
<i>CTF8</i>	<i>URA3</i>	fwd	VIII	486155	486230	TATATACACTTTACACAGAGCGTGAAGTCTGCGCCAAATAACATAAACAAACAACCTC CGAACAACTAAGTACTcggcatcagagcagattgtactg
	<i>URA3</i>	rev	VIII	486709	486631	CTAACCACTAATATAGCCAAAGGAGTGATAGAAAAAGAATTACTACTATCATTTCAG CCCAATAAACAGCTGAAAAAGAAacaccgcagggttaataactg
<i>DEP1</i>	<i>URA3</i>	fwd	I	129210	129269	AACGGCAAAGTACAAGGGAAGGAAGCACAGAAGCAAGAGGAGGCGCATCGATCGTGG CAGcggcatcagagcagattgtactg
	<i>URA3</i>	rev	I	130547	130488	ATAGCGTTTACACATATTTAAGAAATAACAAAAAGAAGTGGTATGGGGTCCAGTGTGG CGGacaccgcagggttaataactg
<i>FPR1</i>	<i>URA3</i>	fwd	XIV	371821	371881	GATACTTACCATAAACATAAAATAAAAAGCAGAAAGCGGCTCAATTGATAGTACTTT GCTTaccaccgcagggttaataactg
	<i>URA3</i>	rev	XIV	372287	372227	TAAAGTAAGCCTTTCACCTAAACTCGAGTATAAGCAAAAAATCAATCAAAAACAAGT AATAcggcatcagagcagattgtactg
<i>INP54</i>	<i>URA3</i>	fwd	XV	204671	204730	ACTGACGTTATCTGTTTCAGACATAAATGAAAACTTCTAGCCTGACAGCCAGATC ACTcggcatcagagcagattgtactg
	<i>URA3</i>	rev	XV	205945	205886	TAAGAGTAGGCTAACAAAGAAGAAAAGTGAGACAAGAAAATACAGCAGGATTCTGAC CGAacaccgcagggttaataactg
<i>KOG1</i>	<i>URA3</i>	fwd	VIII	475924	475999	TAATAGATTATATATATATATATATATATCTCTTTGCGAGCTAAATGAAAGAAAA AAAAAGAAATGGCACATAcggcatcagagcagattgtactg
	<i>URA3</i>	rev	VIII	480750	480672	GAATGCATTGGTTGTAGATTCCCTTGATTACATTAGCGAATCCTATTGCATGCA GAGAAGGGTAAAAGATACATAAacaccgcagggttaataactg
<i>RNR2</i>	<i>URA3</i>	fwd	X	392343	392403	CTCGATTGGCTATCTACCAAGAATCCAACTTAATACACGTATTTATTGTGCCAAT TACCcggcatcagagcagattgtactg
	<i>URA3</i>	rev	X	393664	393604	CGAAAGCCCACATAAAGAGATTGAAGAGACTGCGTAAAAAGAAATATATAGAGAGAT ACTCacaccgcagggttaataactg
	<i>NatMX</i>	fwd	X	392343	392403	CTCGATTGGCTATCTACCAAGAATCCAACTTAATACACGTATTTATTGTGCCAAT TACCcgtacgctgcaggctcgac
	<i>NatMX</i>	rev	X	393604	393664	CGAAAGCCCACATAAAGAGATTGAAGAGACTGCGTAAAAAGAAATATATAGAGAGAT ACTCacgatgaattcgagctcg
<i>RNR4</i>	<i>URA3</i>	fwd	VII	855203	855263	TATATATAAATATATATAAATAAAAGTGGCCAAGAATAAAAGAACGCCCCGCTCGT TGACacaccgcagggttaataactg
	<i>URA3</i>	rev	VII	856362	856302	TACAAAAACAGATCTTTTGGAGCCACACAACCCCGCAACGCACACAATTAGTTAT TACAcggcatcagagcagattgtactg
<i>TOR1</i>	<i>URA3</i>	fwd	X	559355	559415	TCACGAGAGATCATTGGTAAAGTAAACATACATCAACCGCTAGCAGGTTTGCAT TGATcggcatcagagcagattgtactg
	<i>URA3</i>	rev	X	566889	566829	AATGCGTAATACAAAAAATAAATAGTAAACAAAGCACGAAATGAAAAATGACACC GCAGacaccgcagggttaataactg
	<i>NatMX</i>	fwd	X	559355	559415	TCACGAGAGATCATTGGTAAAGTAAACATACATCAACCGCTAGCAGGTTTGCAT TGATcgtacgctgcaggctcgac
	<i>NatMX</i>	rev	X	566829	566889	AATGCGTAATACAAAAAATAAATAGTAAACAAAGCACGAAATGAAAAATGACACC GCAGatcgatgaattcgagctcg
<i>YNR066C</i>	<i>URA3</i>	fwd	XIV	753665	753724	TTCACTACCGTCGCCAACGGAACCTGTCAATTAACATAATTCGGCAGTAGGATTGA GATcggcatcagagcagattgtactg
	<i>URA3</i>	rev	XIV	755095	755036	ATAAAGTTCCGAGCTTTGAAAAAAGCTTTGAACTAAGAAAAGGTAAGAGATCCTCA ATTacaccgcagggttaataactg

## Supplemental References

- Barbera, M. A. and Petes, T. D. (2006). Selection and analysis of spontaneous reciprocal mitotic cross-overs in *Saccharomyces cerevisiae*. *Proc. Natl. Acad. Sci. U.S.A.* *103*, 12819–12824.
- Bates, D., Maechler, M., Bolker, B. M., and Walker, S. (2015). Fitting linear mixed-effects models using lme4. *J. Stat. Soft.* *67*, 1–48.
- DePristo, M. A. et al. (2011). A framework for variation discovery and genotyping using next-generation DNA sequencing data. *Nat. Genet.* *43*, 491–498.
- Fischer, A., Vázquez-García, I., Illingworth, C. J., and Mustonen, V. (2014). High-definition reconstruction of clonal composition in cancer. *Cell Rep.* *7*, 1740–1752.
- Gelman, A. and Hill, J. (2006). *Data analysis using regression and multilevel/hierarchical models*. Cambridge University Press.
- Gerke, J., Lorenz, K., and Cohen, B. (2006). Genetic interactions between transcription factors cause natural variation in yeast. *Science* *323*, 498–501.
- Hamon, A. and Ycart, B. (2012). Statistics for the Luria-Delbrück distribution. *Electron. J. Stat.* *6*, 1251–1272.
- Illingworth, C. J. R., Parts, L., Bergström, A., Liti, G., and Mustonen, V. (2013). Inferring genome-wide recombination landscapes from advanced intercross lines: application to yeast crosses. *PLoS One* *8*, 1–10.
- Illingworth, C. J. R., Parts, L., Schiffels, S., Liti, G., and Mustonen, V. (2012). Quantifying selection acting on a complex trait using allele frequency time series data. *Mol. Biol. Evol.* *29*, 1187–1197.
- Koser, P. L. et al. (1993). The tyrosine89 residue of yeast FKBP12 is required for rapamycin binding. *Gene* *129*, 159–165.
- Lang, G. I. and Murray, A. W. (2008). Estimating the per-base-pair mutation rate in the yeast *Saccharomyces cerevisiae*. *Genetics* *178*, 67–82.
- Li, H. (2011). A statistical framework for SNP calling, mutation discovery, association mapping and population genetical parameter estimation from sequencing data. *Bioinformatics* *27*, 2987–2993.
- Li, H. and Durbin, R. (2009). Fast and accurate short read alignment with Burrows-Wheeler transform. *Bioinformatics* *25*, 1754–1760.
- Liti, G. et al. (2009). Population genomics of domestic and wild yeasts. *Nature* *458*, 337–341.
- Lorenz, M. C. and Heitman, J. (1995). TOR mutations confer rapamycin resistance by preventing interaction with FKBP12-rapamycin. *J. Biol. Chem.* *270*, 27531–27537.
- Lunter, G. and Goodson, M. (2011). Stampy: A statistical algorithm for sensitive and fast mapping of Illumina sequence reads. *Genome Res.* *21*, 936–939.
- Luria, S. E. and Delbrück, M. (1943). Mutations of bacteria from virus sensitivity to virus resistance. *Genetics* *28*, 491–511.
- Rimmer, A., Phan, H., Mathieson, I., Iqbal, Z., Twigg, S. R. F., Wilkie, A. O. M., McVean, G., and Lunter, G. (2014). Integrating mapping-, assembly- and haplotype-based approaches for calling variants in clinical sequencing applications. *Nat. Genet.* *46*, 912–918.
- Sniegowski, P. D., Dombrowski, P. G., and Fingerman, E. (2002). *Saccharomyces cerevisiae* and *Saccharomyces paradoxus* coexist in a natural woodland site in North America and display

different levels of reproductive isolation from European conspecifics. *FEMS Yeast Res.* *1*, 299–306.

Zackrisson, M. et al. (2016). Scan-o-matic: High-resolution microbial phenomics at a massive scale. *G3 Genes—Genomes—Genetics* *6*, 3003–3014.

Zheng, X. F. and Schreiber, S. L. (1997). Target of rapamycin proteins and their kinase activities are required for meiosis. *Proc. Natl. Acad. Sci. U.S.A.* *94*, 3070–3075.